OCEAN APPLICATIONS TEHNICAL NOTE 9.

SIMULATION OF THE TROPICAL PACIFIC OCEAN (1984-93)USING AN OGCM FORCED WITH AGCM (HADAM2b) WIND STRESS.

by

P.Mclean, M.K.Davey, & S.Ineson.

Met Office
FitzRoy Road, Exeter, Devon. EX1 3PB

Simulation of the Tropical Pacific Ocean (1984-93) using an OGCM forced with AGCM (HADAM2b) Wind Stress

By PETER McLEAN, MICHAEL K. DAVEY and SARAH INESON, Hadley Centre, Meteorological Office, London Road, Bracknell, RG12 2SY.

ABSTRACT

Changes of sea surface temperature (SST) in the tropical Pacific Ocean can be modelled using wind stress forcing fields. The skill of simulating both climatology and interannual variability is dependent on both the model and the forcing fields used. This report describes the results of using wind stress fields from a version of the Hadley Centre atmosphere general circulation model (AGCM), HADAM2b, to force a tropical Pacific Ocean general circulation model (OGCM), and compares these results to observations. A four year spin-up was first carried out using the climatological AGCM wind stresses, the results show that the central equatorial Pacific is colder than observed climatology by 2°C in September, and the eastern boundary was warmer than observed climatology. The interannual variability was simulated forced by AGCM wind stresses (1983-94). The low frequency interannual variability of SST was well simulated in the west Pacific but was masked at times by high frequency events, especially in the 1990s when several large anomalous westerly windburst events occurred. These events caused a rapid warming of the sea surface in the central west Pacific and also generated equatorial Kelvin waves. The SSTs at the eastern boundary were poorly simulated compared to a similar experiment carried out using FSU winds as forcing fields.

Ocean Model Description

A Bryan/Cox type of ocean general circulation model (Cox, 1984) is used with a variable finite difference spatial grid. The meridional grid spacing is 1/3° along the equator increasing to 1° at the boundaries at 30° north and south. The zonal grid spacing is 1.5° over most of the ocean decreasing to about 0.5° at the closed eastern and western boundaries. There are 16 levels at 5, 15, 25, 35, 48, 67, 96, 139, 204, 301, 447, 666, 996, 1490, 2232 and 3339 m. The parameters used are those listed by Bell (1994) for this particular OGCM. For computational efficiency the barotropic mode is omitted as the barotropic currents are small in the tropics. There is no variation in bottom topography. The horizontal eddy viscosity decreases with grid spacing with a minimum value of 2×10^3 m^2s^{-1}. Diffusivity for temperature and salinity is constant at 2×10^3 m^2s^{-1} over most of the ocean increasing to 3×10^4 m^2s^{-1} near the open northern and southern boundaries. Temperature and salinity at these open boundaries are kept close to their seasonally varying climatological values (Levitus, 1982). Short wave radiation is allowed to penetrate below the top model layer, attenuated using a two band approximation. Two types of vertical mixing are used. Richardson number dependent diffusivity is applied with $V_b = 0.5 \times 10^{-4}$ m^2s^{-1}, $K_b = 0.05 \times 10^{-4}$ m^2s^{-1} and $V_o = 55 \times 10^{-4}$ m^2s^{-1}. A Kraus/Turner mixing scheme (Kraus and Turner, 1967) is embedded in the model principally to represent surface-generated turbulence (Ineson and Gordon, 1989).

1. Climatology

The model was spun up from rest using temperature and salinity from September climatology (Levitus, 1982) as an initial state. The momentum forcing fields were 10 year mean monthly wind stresses (1984-93) produced from one realization of HADAM2b, which was forced with observed SSTs from Global ice and SST data(GISST 1.1) (Parker et al, 1994). Surface heat flux Q is calculated as

$$Q = Q_0 - (dQ/dT)_0 (T_0-T)$$

where T is model SST, Q_0 and T_0 are monthly climatological heat flux and SST and $(dQ/dT)_0$ is an estimate of the dependence of Q on changes in SST. The climatological values are taken from Oberhuber (1988). The salinity S is controlled by forcing surface salinities toward observed values using

$$F = F_0 + \lambda(S_0-S)$$

where F is the net surface fresh water flux (precipitation - evaporation), and F_0 is a climatological value (evaporation from Esbensen and Kushnir (1981) and precipitation from Jaeger, (1976)). S_0 is a climatological surface salinity (Levitus, 1982) and $\lambda = (35\ W/m^2/K)/(S_{00}\ C_p)$ where S_{00} is 0.035, a standard salinity value and C_p is specific heat. The upper tropical ocean in the model was close to equilibrium after 3 years of integration, results in this section are for year 4.

1.1 Wind Stress

Figs. 1.1 and 1.2 show mean wind stress plots for March and September comparing AGCM wind stresses with a climatology derived from the FSU pseudo-stress dataset. A drag coefficient of 0.75 x 1.535 x 10^{-3} was chosen to convert the FSU winds to stresses. The factor 1.535 x 10^{-3} gives average wind stress values close to the Hellerman/Rosenstein climatology (Stockdale, 1992), but these values are known to be too strong in the tropics and so they are reduced by a factor of 0.75. The main patterns of low level tropical Pacific circulation can be identified; the north-easterly trade winds converge in areas of low wind speed to the north of the equator in the central and east Pacific and over the west Pacific equatorial warm pool region. The north easterlies (south easterlies) are strongest in March (September). The easterly component of the AGCM wind stresses are more than 25% larger between 110 and 160°W near the equator than the FSU wind stresses in September. This is seen in Fig. 1.3 (b) which shows the difference between the two. The easterly winds are also stronger in March, south of the equator in the central east Pacific (100-120°W). Also there is a large easterly bias in the west Pacific poleward of the latitude of 10° in the southern (northern) hemisphere in September (March), with a westerly bias equatorward of 10°.

Fig. 1.4 shows the average annual cycle of AGCM and FSU zonal wind stress averaged over the central equatorial Pacific, 5°N-5°S, 165-225°E and shows that the amplitude of the seasonal cycle is greater for the AGCM wind stresses, with a weaker easterly component from November to May and stronger from June to October.

1.2 Sea Surface Temperature

Figs. 1.5 and 1.6 show SST plots for the OGCM and observations from Levitus (1982). The ocean model simulates the main features of the SST distribution reasonably well. The warm pool in the west Pacific migrates seasonally to remain in the southern (northern) hemisphere in March (September) and in the east Pacific SSTs are colder with the equatorial cold tongue prominent in September. Comparison shows that in the southern (northern) hemisphere in March (September) there are anomalously high SSTs in the west Pacific, and the east Pacific. In the central equatorial Pacific there is a cold anomaly compared to climatology, which is most noticeable in the September plot (Fig. 1.6). Note that in September the model cold tongue has become separated from the coast by warmer water. A plot showing the difference between the simulation and climatological SSTs from Levitus (1982), Fig. 1.7, shows that the magnitude of the cold anomaly in the central Pacific is up to 2°C in September. In March the anomaly, now situated further east, is about 1°C. In both months the eastern boundary was too warm by as much as 4°C around 5°S, and the west Pacific is at least 1°C too warm over a large area.

1.3 Temperature Profile

Fig. 1.8 shows temperature against depth along the equator for March and September, along with the 20°C isotherm from the NMC 'ra3' analysis which was produced using a tropical Pacific OGCM with temperature data assimilation (Smith & Chelliah, 1995, Ji et al, 1995). The NMC 20°C isotherm is closer to the surface than in the OGCM in March, especially in the eastern part of the basin. A comparison with the NMC analysis, not shown here, shows that the OGCM thermocline is too diffuse especially in the east. In September the NMC 20°C isotherm is closer to the surface than in the OGCM in the west Pacific, however the thermocline gradient is steeper for the OGCM than the NMC analysis between 100 and 150°W and therefore the 20°C isotherm in the east Pacific is comparable with the NMC analysis. The steeper thermocline in September is the result of the anomalously large values of AGCM wind stress in the central east Pacific at this time. Temperature profiles are also shown for the same two months along 150°W in Fig. 1.9. The seasonal cycle of the North Equatorial Counter Current is simulated well as indicated by the steeper isotherm in September than in March between 5°N and 10°N. The mixed layer depth is deeper in September around 10°S than in March indicating more wind mixing in this region at this time, consistent with wind climatology (Figs 1.1 and 1.2).

1.4 U, V and W components of current

The main circulation features are shown in Figs. 1.10-1.14. In general the main surface features compared well with those observed by shipdrift data (Roberts, 1995). In Fig. 1.10 the surface westward current along the equator was found to be stronger in September than for March showing the result of the larger easterly September wind stresses. The equatorial undercurrent has a maximum velocity of 80 cms^{-1}, occurring around 75 m between 120 and 100°W in March. In September it is 90 cms^{-1} occurring around 125 m between 110 and 130°W. Note that the undercurrent does not reach the surface in the east Pacific, unlike observations. The vertical velocity profiles along the equator, Fig. 1.11, show the upwelling extending from the east Pacific into the central Pacific with stronger upwelling in September. There also appears to be subsurface downwelling in the east Pacific in March

which is possibly a model error. It extends from 25 m to 125 m at 80°W and reduces further west and deeper in the ocean. In September weaker downwelling occurs further west and deeper than in March. The velocity profiles along 150°W in Figs. 1.12-1.14 show more intense circulations near the equator in September than March. The south equatorial current is greater as the equatorial easterlies are stronger in September than in March, and the North Equatorial Counter Current is greater in September in agreement with the observed seasonal cycle. At 150°W the Equatorial Undercurrent occurs below about 50 m with a maximum velocity of 40 cms^{-1} in March and 80 cms^{-1} in September occurring at about 150 m. The meridional velocity plots in Fig.1.13 show how.the strong easterly winds in September along the equator cause greater Ekman divergence which leads to more upwelling at the equator, with greater downwelling either side of the equator as shown in Fig.1.14 (b).

1.5 20°C Isotherm Depth

Fig. 1.15 shows the mean 20°C isotherm depth (d20) for March and September. A comparison made with the NMC analysis (Ji and Smith (1995) Fig. 4), shows general agreement with the shallowest depth in the east Pacific, the deepest in the subtropical gyres and a ridge along 10°N. There was a deeper d20 than in the NMC analysis in the west Pacific and shallower depth in the central Pacific in September, probably associated with the large upwelling in this central area shown by the vertical velocity profile in Fig.1.11 (b). Further, the stronger AGCM winds cause a larger east to west sea level difference with a steeper underlying thermocline slope.

2. Interannual Variability

Monthly mean wind stresses from HADAM2b from May 1983 to May 1994 were next used to force the ocean model which was run from June 1983 to March 1994. The surface heat flux formulation for the interannual experiment was modified to

$$Q = Q_0 - (dQ/dT)_0 (T_0-T_m) - 0.3 (dQ/dT)_0 (T_m-T)$$

where T_m is the monthly mean OGCM climatology. Anomalies from the model seasonal cycle are thus weakly damped, with the factor 0.3 chosen such that the interannual SST anomalies have similar magnitude to those observed.

2.1 Wind Stress Anomaly

Figs. 2.1 and 2.2 show plots of the AGCM wind stress anomaly and the 7 month running mean respectively over the 10 year period. A general eastward propagation trend with a period of approximately two years can be seen in Fig. 2.2. Fig. 2.1 shows the occurrence of several short-lived windbursts generated spontaneously by the AGCM, however the low frequency behavior shown in Fig. 2.2 in the running mean is comparable to that of the FSU analysis (not shown). A comparison of area average AGCM and FSU zonal wind stress anomalies in the central Pacific region (5°N-5°S, 165-225°E) in Figs. 2.3 and 2.4 again show how noisy the AGCM wind stresses are; note in particular the strong bursts at the end of 1991 and during 1992. Interannual variations are less evident in the

AGCM compared to the FSU data.

2.2 Timeseries SST Anomaly Plots

Time series plots of SST anomalies from the 10 year mean (1984-93) for three commonly used areas known as Nino 1+2, 3 and 4 are shown in Figs 2.5 and 2.6. A comparison was made between the simulation using AGCM wind stresses, the observations from GISST 1.1 (Parker et al, 1994), and the simulation using the FSU derived wind stresses (Davey et al, 1994). The root mean squared difference between simulated and observed SST was slightly greater for the AGCM simulation in the combined Nino 1 and 2 area (0-10°N, 90-80°W), but the two were almost the same for the Nino 3 (5°N-5°S, 90-150°W) and Nino 4 (5°N-5°S, 160°W-150°E) areas. The correlation coefficient was lower for the AGCM simulation in all three areas, particularly in the Nino 1+2 area where the model with AGCM winds simulated false cold events in 1984 and the end of 1992. The warm event of 1987 was underestimated, as well as the cold event in 1988, the warm events of 1992 and 1993 were missed. The AGCM simulation for Nino 3 underestimated the warm events of 1987 and 1991, and missed the cold event of 1988, with a false cold event occurring in 1992. The Nino 4 area was better simulated, with a short false cooling in 1990 and a false warming in 1993, probably due to the windburst in this area at the end of 1992 shown in Fig. 2.2. Overall the AGCM simulation was noisy, and some errors may be attributed to simulated short term events.

2.3 Equatorial Sea Surface Temperature Anomaly

Fig. 2.7 shows a plot of simulated SST anomalies along the equator over the ten year period, while Fig 2.8 shows observed GISST anomalies from the 1984-93 mean. Simulated SST anomalies generally agree with the characteristics of the observations up to 1990, a short-lived cool event occurred in the simulation in 1990 followed by a sequence of intense events in 1992 and 93. The difference between the simulation and observations is shown in Fig. 2.9 and several episodes with differences of greater than 2°C are locally observed. However, the most noticeable feature is a large warm anomaly in the central Pacific in 1992-3. Fig 2.7 shows that the simulation is fairly noisy suggesting the AGCM wind bursts may have triggered local disturbances in SST, and so a 7 month running mean of the simulation was taken and compared with observations, Figs. 2.10 and 2.11. These show that the low frequency SST anomalies were simulated fairly well except during 1988 when the OGCM underestimates the cold anomaly in the central east Pacific and 1993 when the OGCM is too warm in the central Pacific.

The standard deviation of SST anomaly for the AGCM and FSU forced runs in Figs 2.12 and 2.13 is compared with that observed in Fig 2.14. In all three, variability is largest in the equatorial strip, extending from the east into the west Pacific. The maxima for the observations and the AGCM-forced simulation are near 140°W whereas FSU-forced simulation has a maximum farther west near the dateline. Other maxima occur at the eastern boundary in all three cases. The FSU and AGCM simulation; both miss some of the interannual variability that occurs away from the equator.

2.4 Heat Content

Figs. 2.15 and 2.16 show plots of equatorial depth average temperature (0-360m) anomalies for the simulation and NMC ra3 analysis at the equator representing the heat content evolution over the 10

year period. On a multiseasonal timescale the AGCM-forced simulation is broadly similar to the analysis for 1984-90, with slow eastward movement of anomalies that envelope shorter faster features. After 1990 the AGCM-forced simulation is dominated by strong fast features. Fig. 2.15 shows that the windbursts in Fig.2.1 have a more pronounced signature at the subsurface than at the surface. These windbursts cause eastward propagating Kelvin-like waves with a speed of 0.8-1.5 m/s. There is also evidence of Rossby-like waves to the west of the sharp westerly anomalous windbursts of 1992. Other large anomalies occur in the west in the analysis which are not simulated by the OGCM, the most notable occurring at the end of 1988.

Fig. 2.17 shows how heat content varied over 10 years at 8°N and shows the anomalies tend to move westward with a period of about two years. A notably large anomaly occurred in late 1992 to early 1993 in the west Pacific, this was due to a large westerly windburst at 165°E in October 1992.

Conclusions

The spin up of an OGCM using climatological fields, forced by mean AGCM wind stresses (1984-93) showed some systematic errors. The main error is in the central equatorial Pacific, which was too cold especially in September when anomalies from the Levitus climatology were -2°C over a wide area. The reason for this is that the AGCM wind stresses in this region are too strong in July to October and increase the ocean circulation, in such a way as to produce strong upwelling that extends too far west. By contrast the western and eastern boundaries in the summer hemisphere are always too warm. The warmer eastern boundary is a result of either weak upwelling as seen in Fig 1.11, or upwelling of too warm water such as in Fig. 1.8 (a). Although the thermocline is more diffuse than observed, the circulation features are simulated well, and are stronger in September than March.

The OGCM was forced with monthly mean monthly AGCM wind stresses from May 1983 to May 1994. Interannual variability in the west Central Pacific (Nino 4) region was simulated well up until 1992 when a spurious warming occurred. Further towards the east (Nino 3, Nino 1+2) the variability seemed to be less well captured with some observed warm and cold events being underestimated and false warmings and coolings occurring. The simulated was rather noisy and so a 7 month running mean was applied to the SST data. The filtered results suggested that the low frequency variability was captured reasonably well except during 1988 when the main cooling occurred in the central west rather than the central east Pacific and during 1992 when the warm anomaly in the central west Pacific was pronounced.

The short-lived anomalies in the OGCM simulation can be attributed to short term events in the forcing dataset. The AGCM winds were rather noisy in comparison with the FSU dataset and windbursts simulated by the AGCM generated eastward propagating Kelvin-like waves with a clear sub-surface signature. The large windbursts in 1992 may have been influenced by the SST used to force the AGCM as the observed GISST values show some large warm anomalies in the central Pacific at this time.

Despite the noisy and biased winds produced in this version of the AGCM, the interannual OGCM behaviour was, overall, reasonably realistic. The noise could be reduced in a simulation by using an ensemble of AGCM experiments. Similar ensembles of coupled GCM experiments may also be required to reduce the impact of spontaneous AGCM wind bursts in predictions. To avoid substantial impact of random windbursts from an overactive AGCM on ocean simulations or CGCM runs, it may be necessary to filter the AGCM surface stresses in some way.

Acknowledgment - We would like to thank Maria Noguer for providing the AGCM data.

References

Bell M.J. 1994. Notes on how to choose parameter values for the Cox numerical ocean circulation model. Forecasting Research Tech. Rep. No.135, UK Meteorological Office, Bracknell.

Cox, M.D. 1984. A primitive equation, 3-dimensional model of the ocean. GFDL Ocean Group Tech Rep. 1, Geophys. Fluid Dyn. Lab/NOAA, Princeton. NJ, USA.

Davey M.K., S Ineson and M.A. Balmaseda 1994. Simulation and hindcasts of tropical Pacific Ocean and interannual variability. Tellus 46a, 433-447.

Esbensen. S.K. and Y. Kushnir 1981. The heat budget of the global ocean: an atlas based on estimates from marine surface observations. Rep. no.29, Climate Res. Inst, Oregan State University, Corvallis.

Goldenberg S. D. and J.J. O'Brien 1981. Time and space variability of tropical Pacific wind stress. Mon. Weath. Rev. 109, 1190-1207.

Ineson S. and C. Gordon 1989. Parameterization of the upper ocean mixed layer in a tropical ocean GCM. Dynamical Climatology Technical Note No. 74, UK Meteorological Office, Bracknell.

Jaeger L. 1976. Monthly maps of precipitation for the world ocean. D. Wetterd. Ber. 18, no.139.

Ji M., A. Leetmaa and J Derber 1995. An ocean analysis system for seasonal to interannual climate studies. Mon. Weath. Rev., 123, 460-481.

Ji M. and T. M. Smith 1995. Ocean model response to temperature data assimilation and varying surface wind stress: Intercomparisons and implications for climate forecast. Mon. Weath. Rev., 123, 182-1821.

Kraus E.B. and J.S. Turner 1967. A one-dimensional model of the seasonal thermocline. Part II. Tellus 19, 98-105.

Levitus S. 1982, Climatological atlas of the world ocean. NOAA Prof. Paper No.13.

Oberhuber J.M. 1988. An atlas based on the COADS dataset. Max Planck-Institut für Meteorologie Report no. 15.

Parker D.E., C.K. Folland, A. Bevan, M.N. Ward, M Jackson and K. Maskell 1994. Marine surface data for analysis of climatic fluctuations of interannual to century timescales. In Natural Climate Variability on decade-to-century timescales, (Martinson D.G et al (editors)) National Academy Press, Washington D.C., U.S.A.

Roberts C.M. 1995, A 1 degree by 1 degree climatology of surface currents derived from ship drift data. Ocean Applications Internal Paper 1, UK Meteorological Office, Bracknell.

Smith T.M and M. Chelliah (1995), The annual cycle in the tropical Pacific Ocean based on assimilated ocean data from 1983 to 1992, J. Clim., Vol. 15, 1600-1614.

Stockdale T. 1992. Simulation and prediction of tropical SST with a coupled ocean-atmosphere model, DPhil thesis, Oxford University, UK.

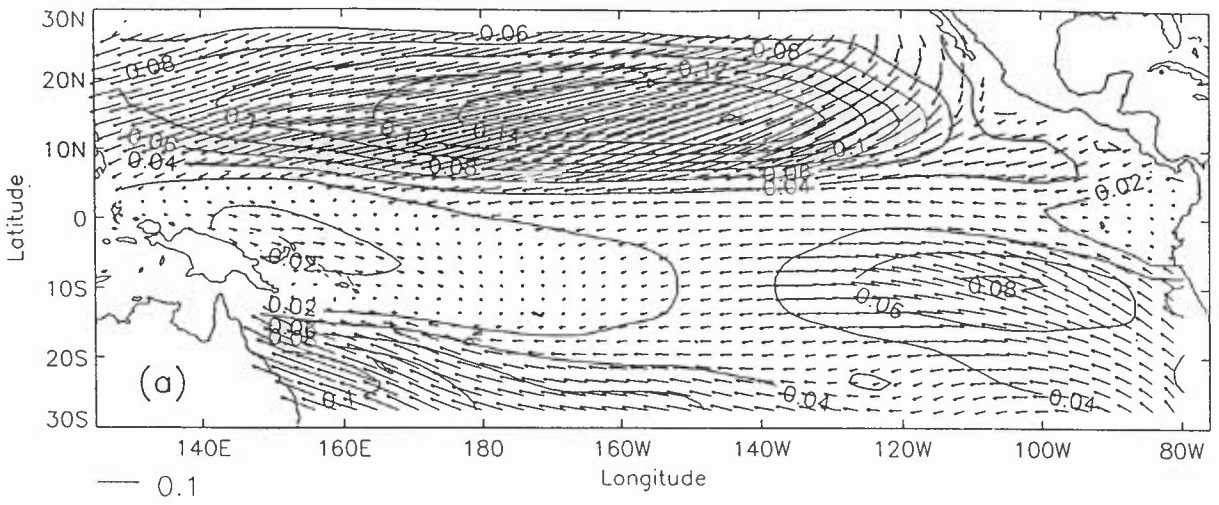

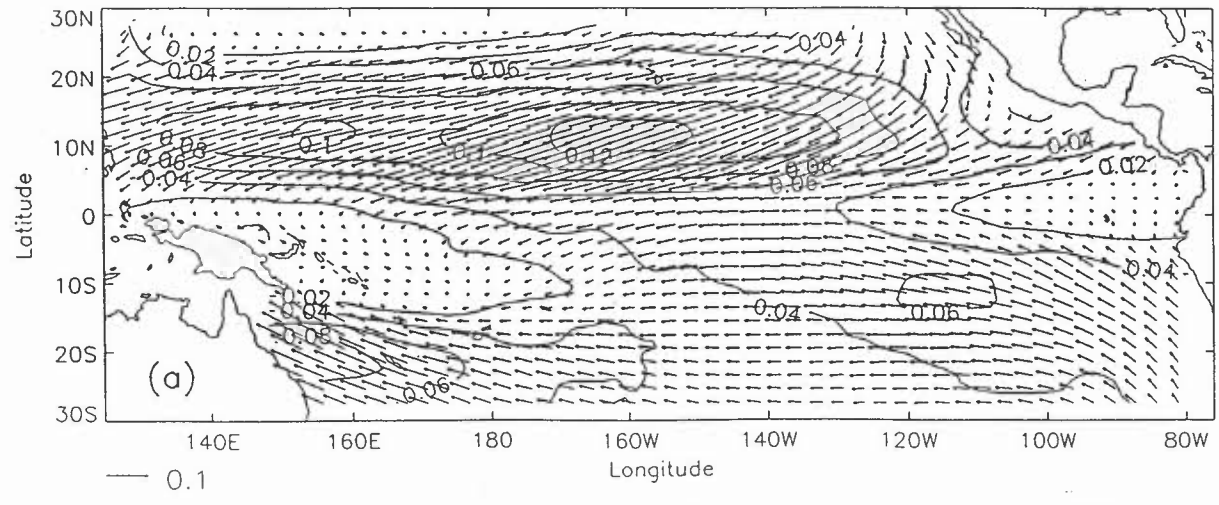

Fig.1.1 Mean Wind Stresses (Nm^{-2}) for March (a) AGCM (b) FSU

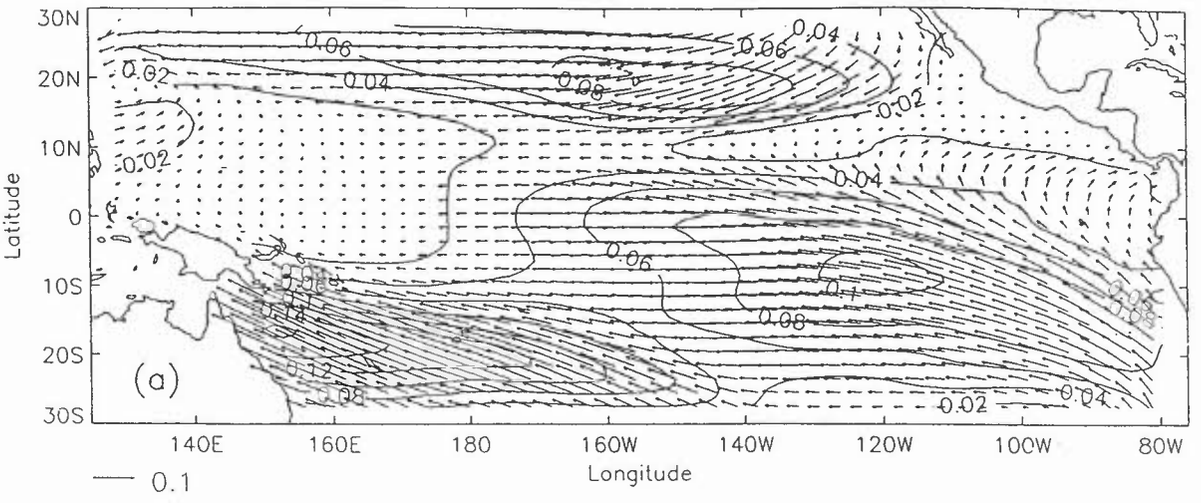

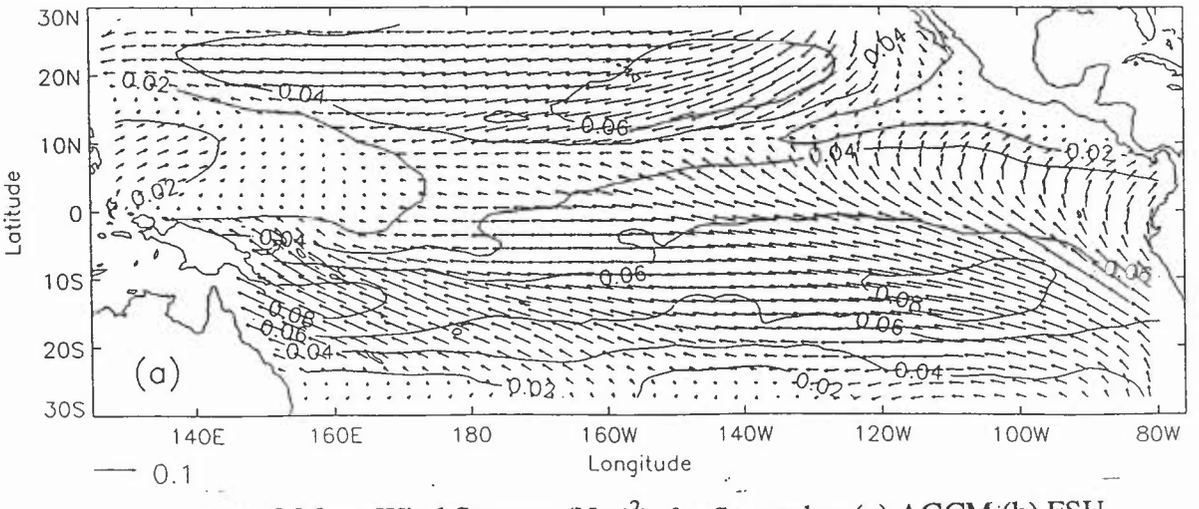

Fig.1.2 Mean Wind Stresses (Nm^{-2}) for September (a) AGCM (b) FSU

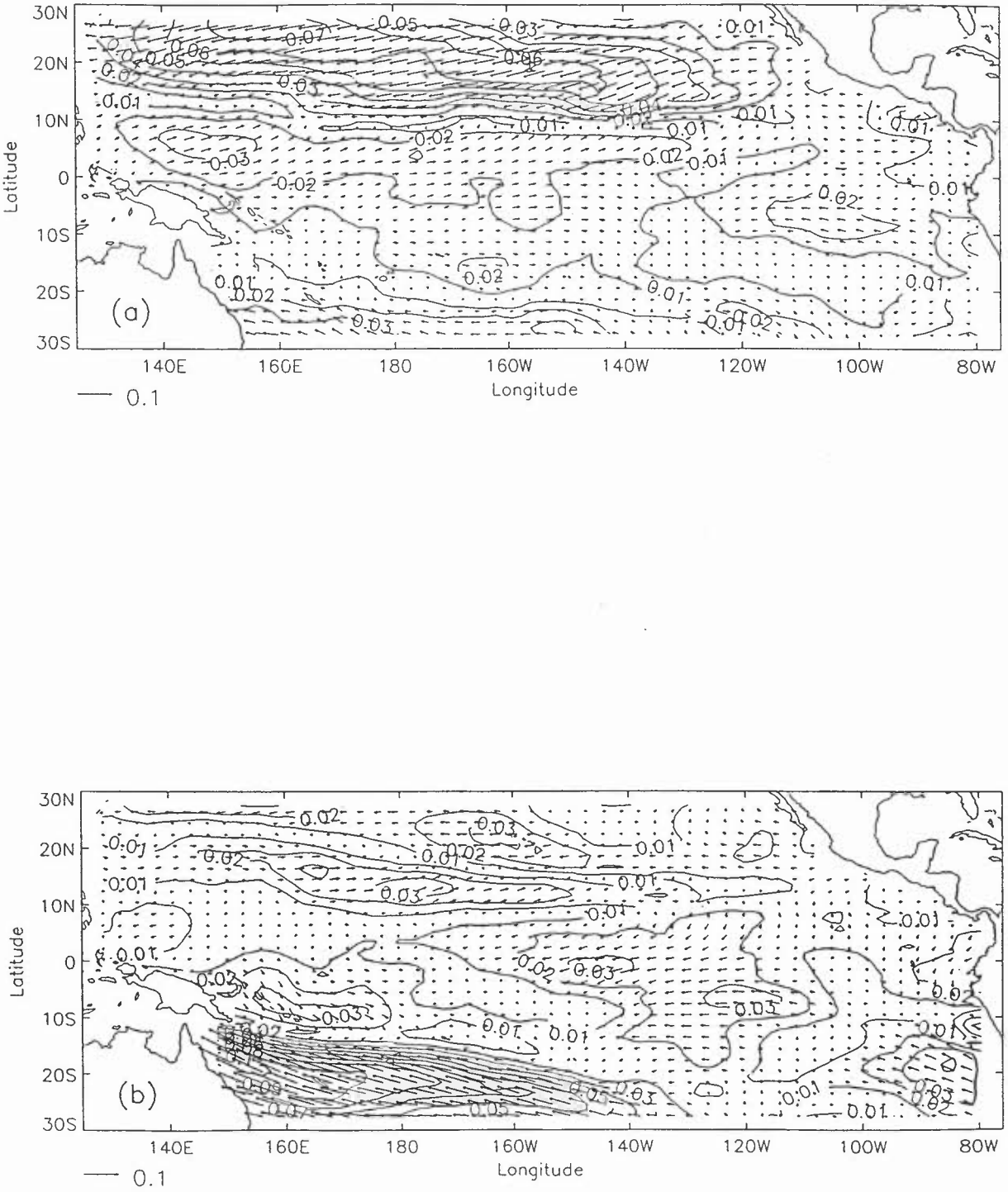

Fig 1.3 AGCM - FSU Wind Stresses (Nm^{-2}) for (a) March (b) September

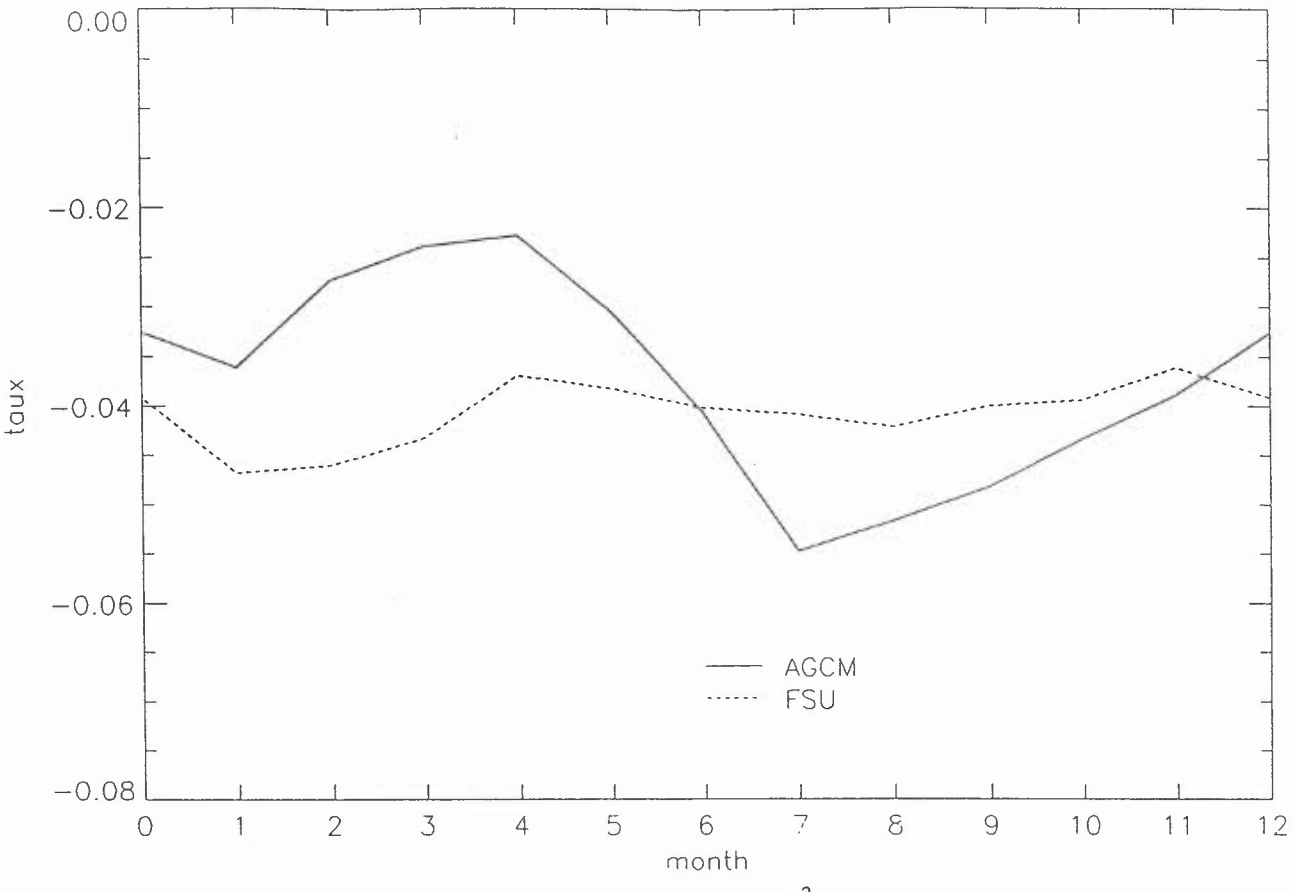

Fig.1.4 Mean Annual Cycle of Zonal Wind Stress (Nm^{-2}) for the AGCM and FSU Dataset in the Region 5°N-5°S, 165°E-225°E

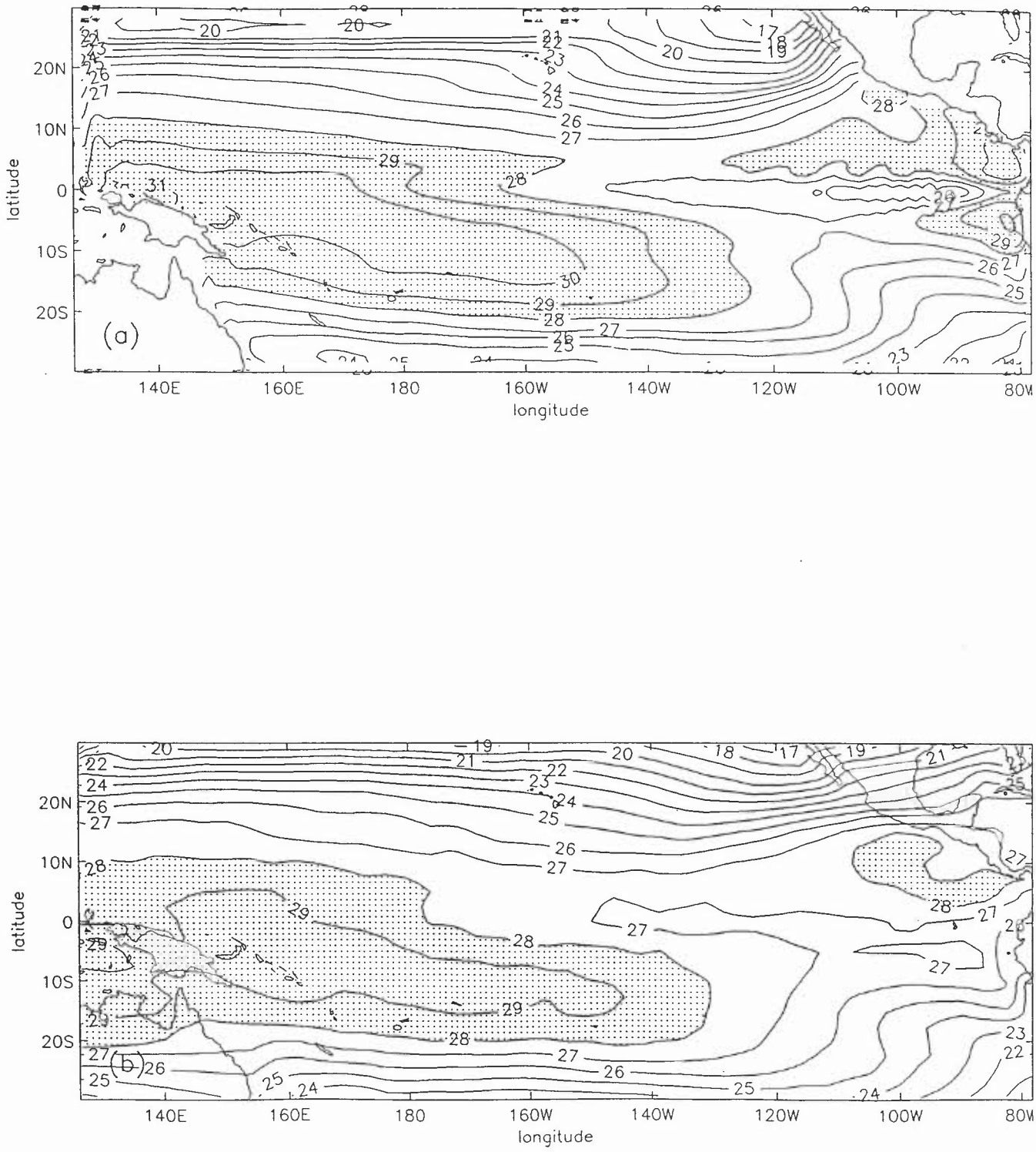

Fig. 1.5 SST Climatology (°C) of (a) GCM and (b) Levitus for March.

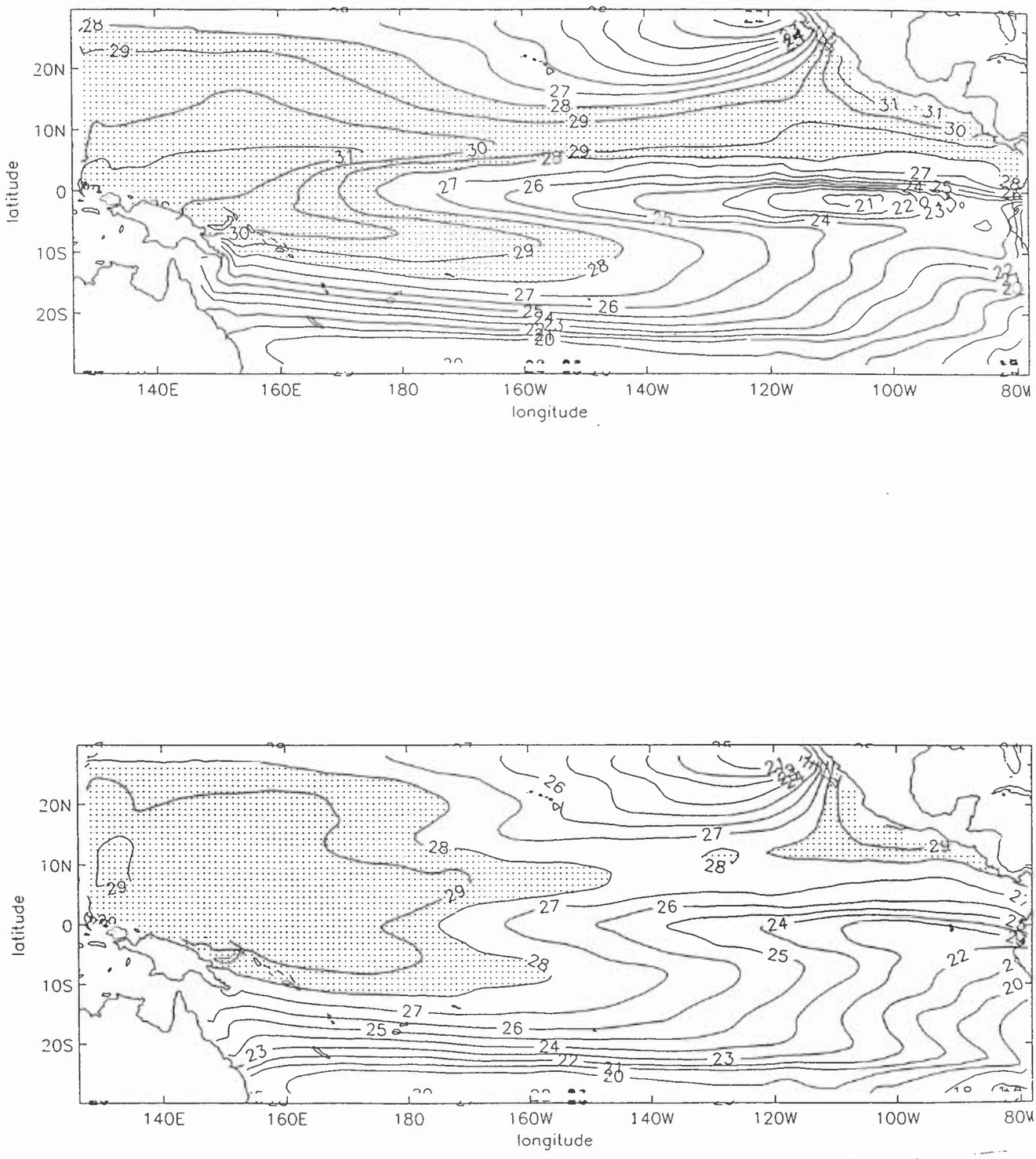

Fig.1.6 SST Climatology (°C) for (a) GCM and (b) Levitus for September

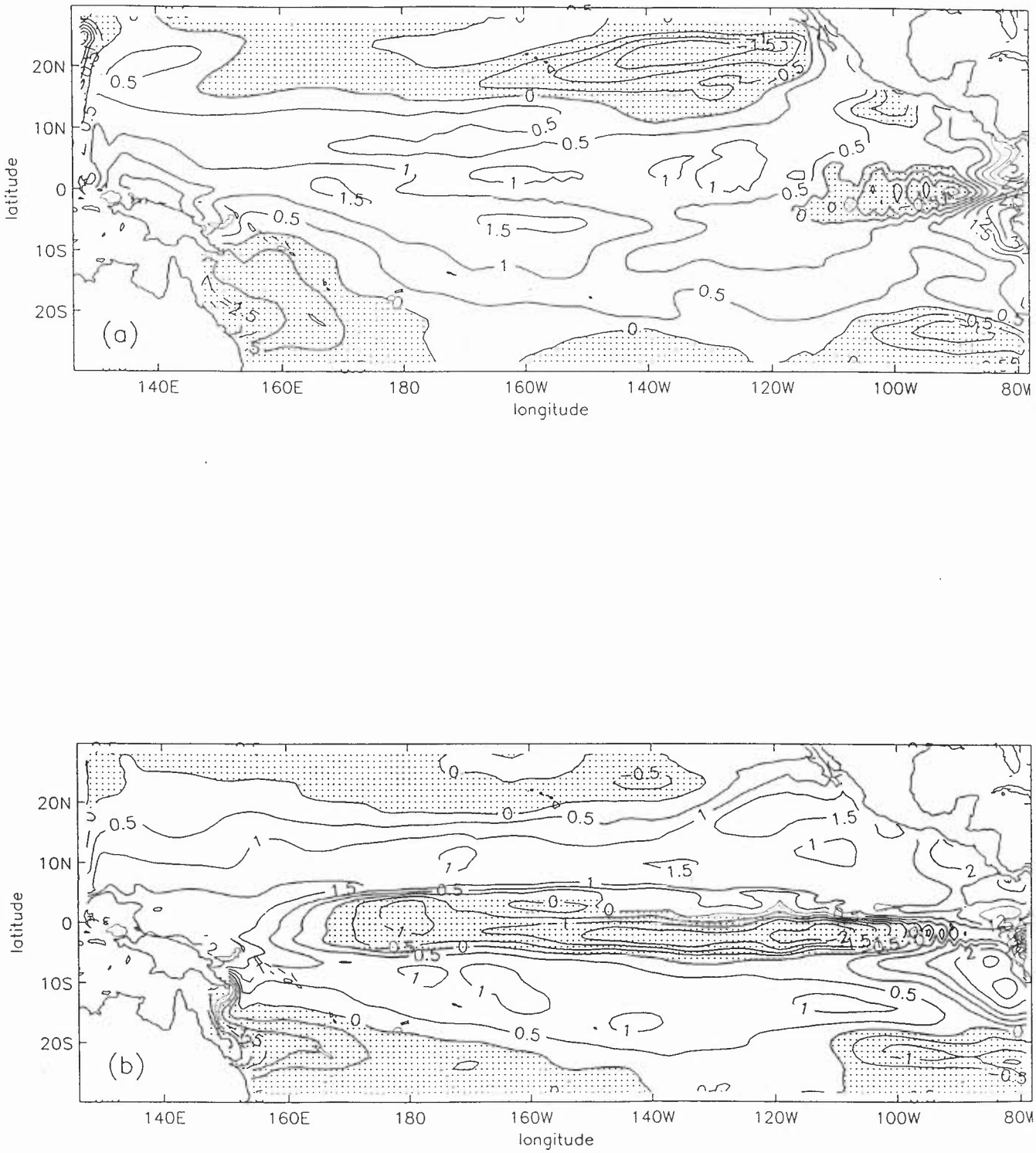

Fig. 1.7 GCM - Levitus Climatology (°C) for (a) March and (b) September.

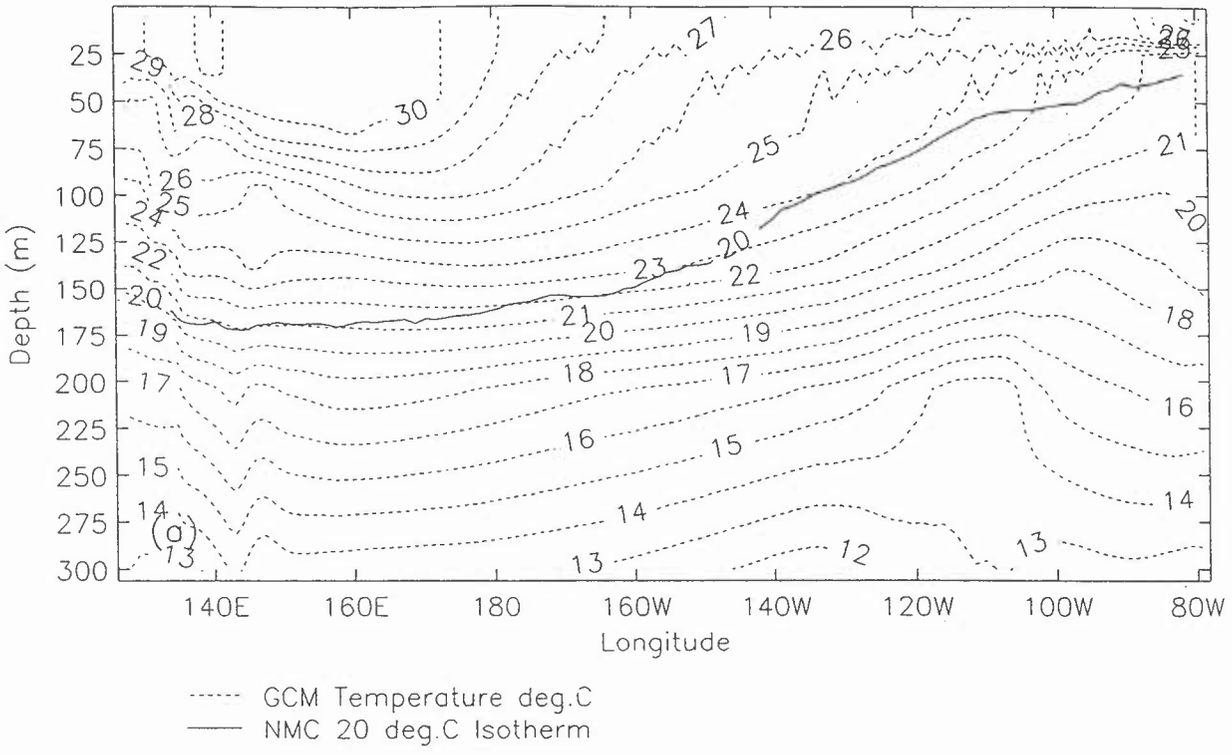

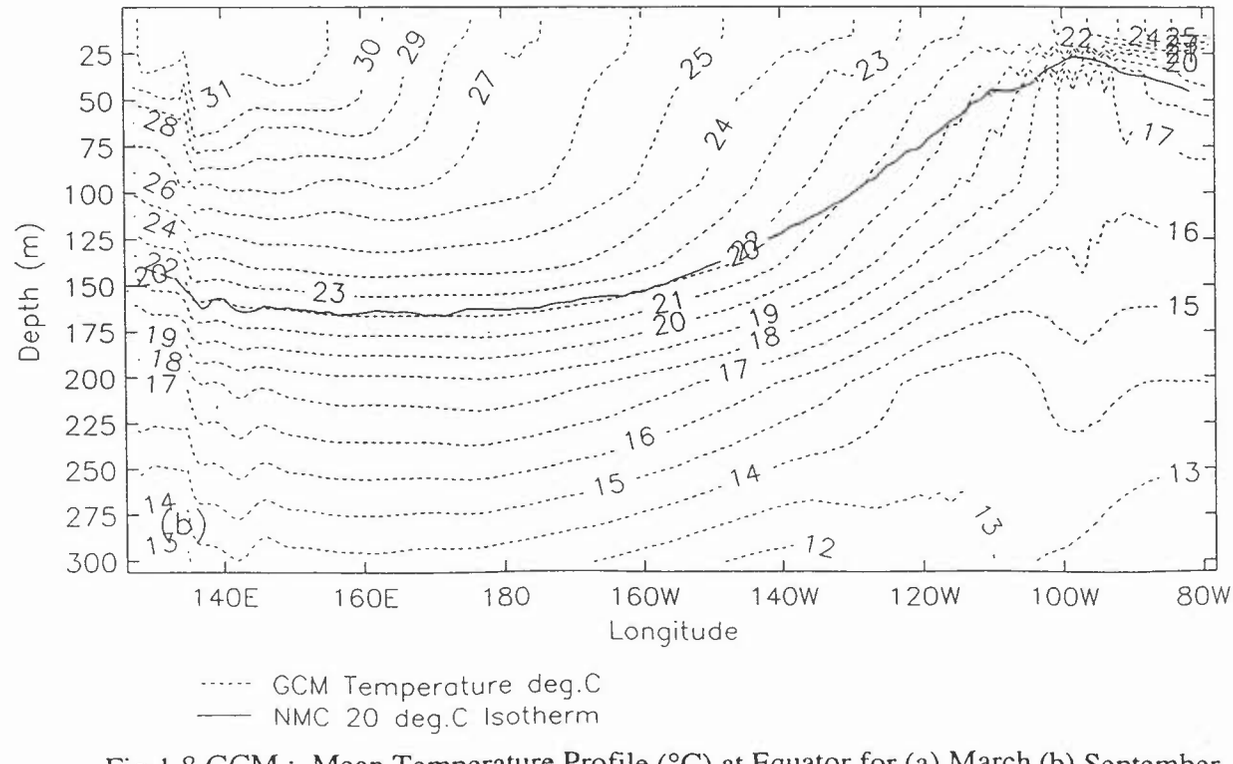

Fig.1.8 GCM : Mean Temperature Profile (°C) at Equator for (a) March (b) September

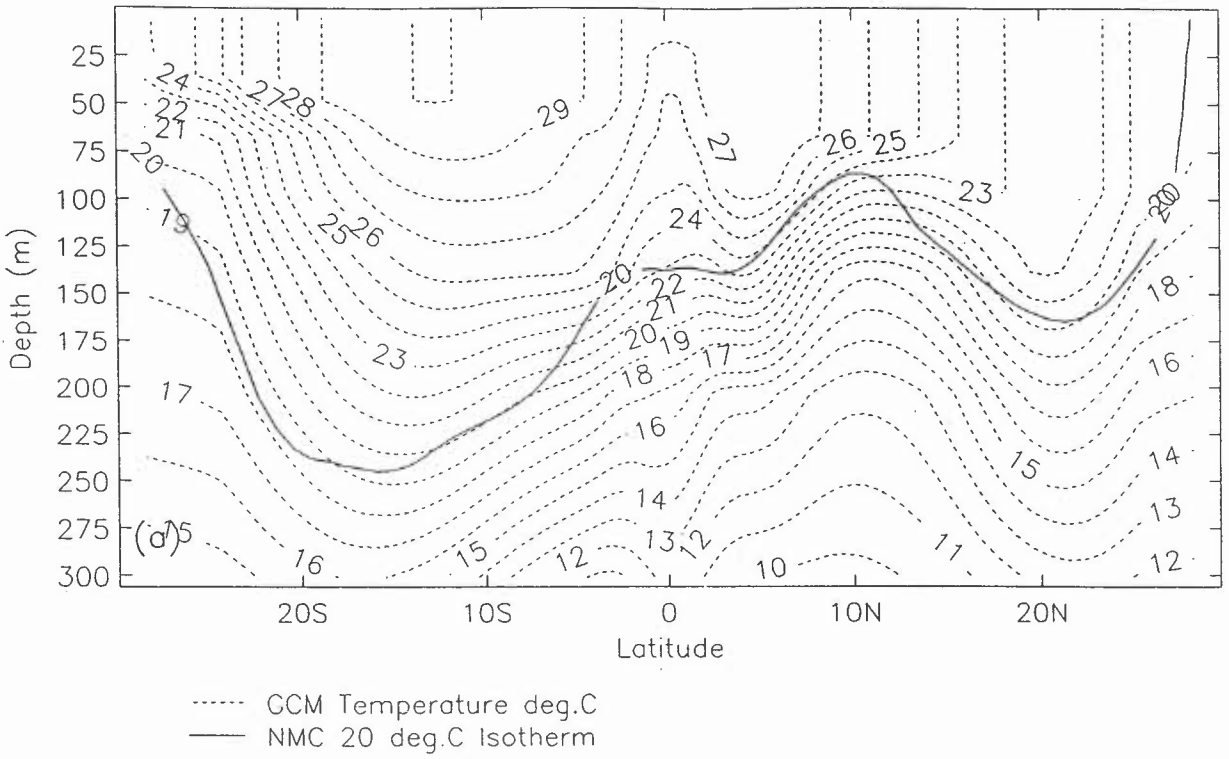

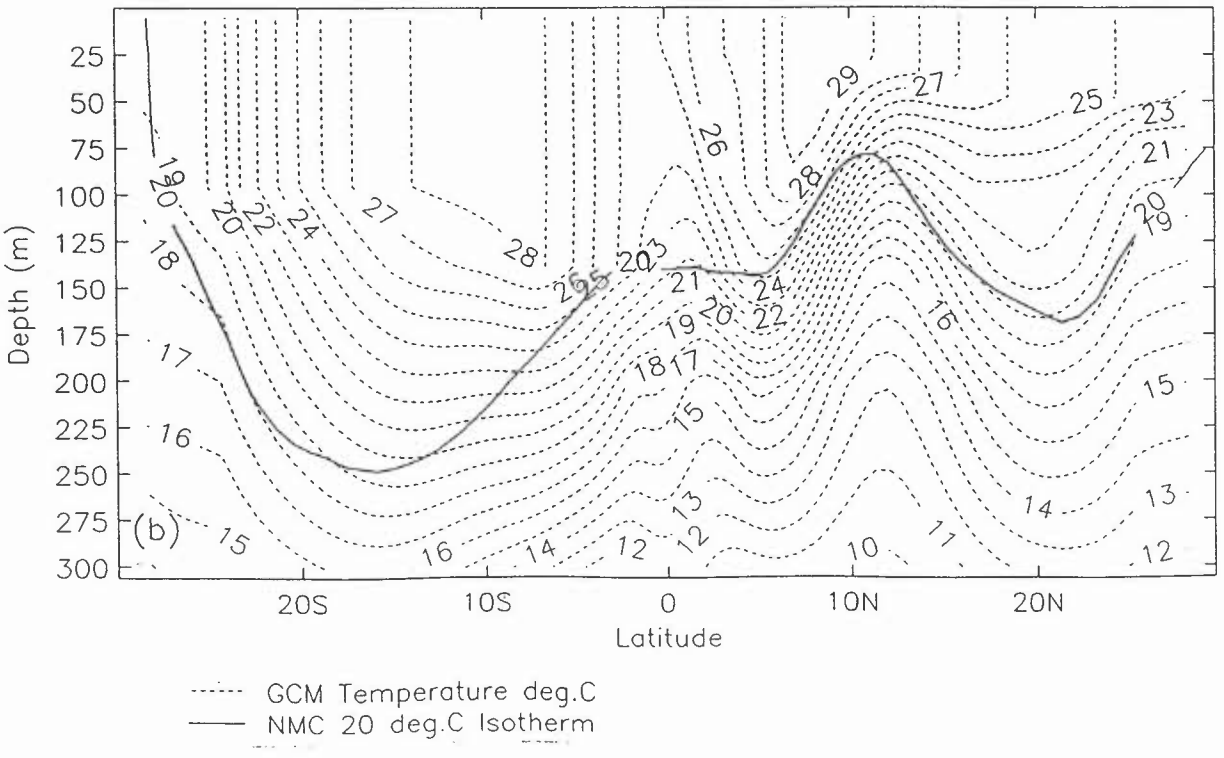

Fig.1.9 GCM : Mean Temperature Profile (°C) at 150°W for (a) March (b) September

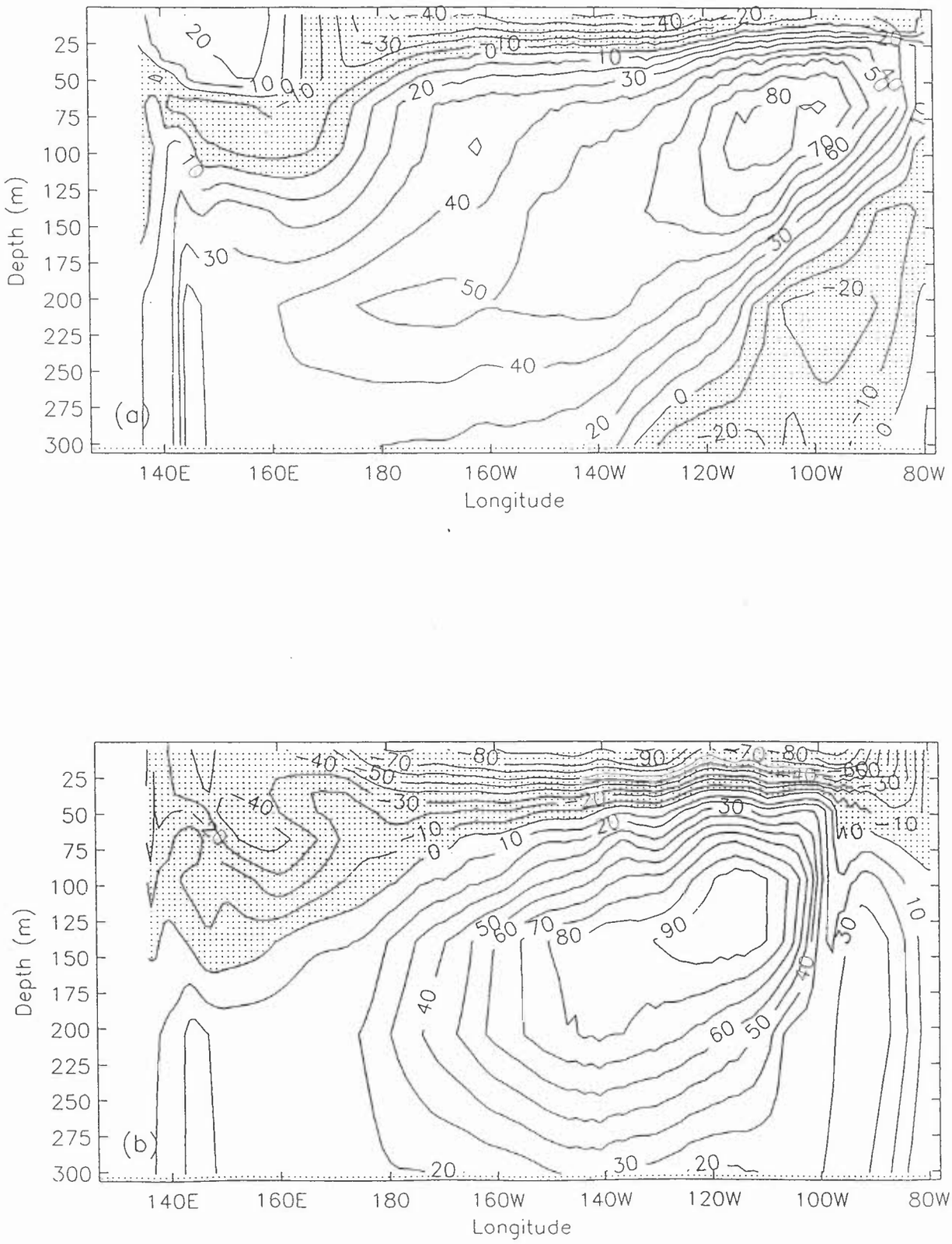

Fig.1.10 GCM : Mean Baroclinic Zonal Velocity (cms^{-1}) at Equator for (a) March (b) September

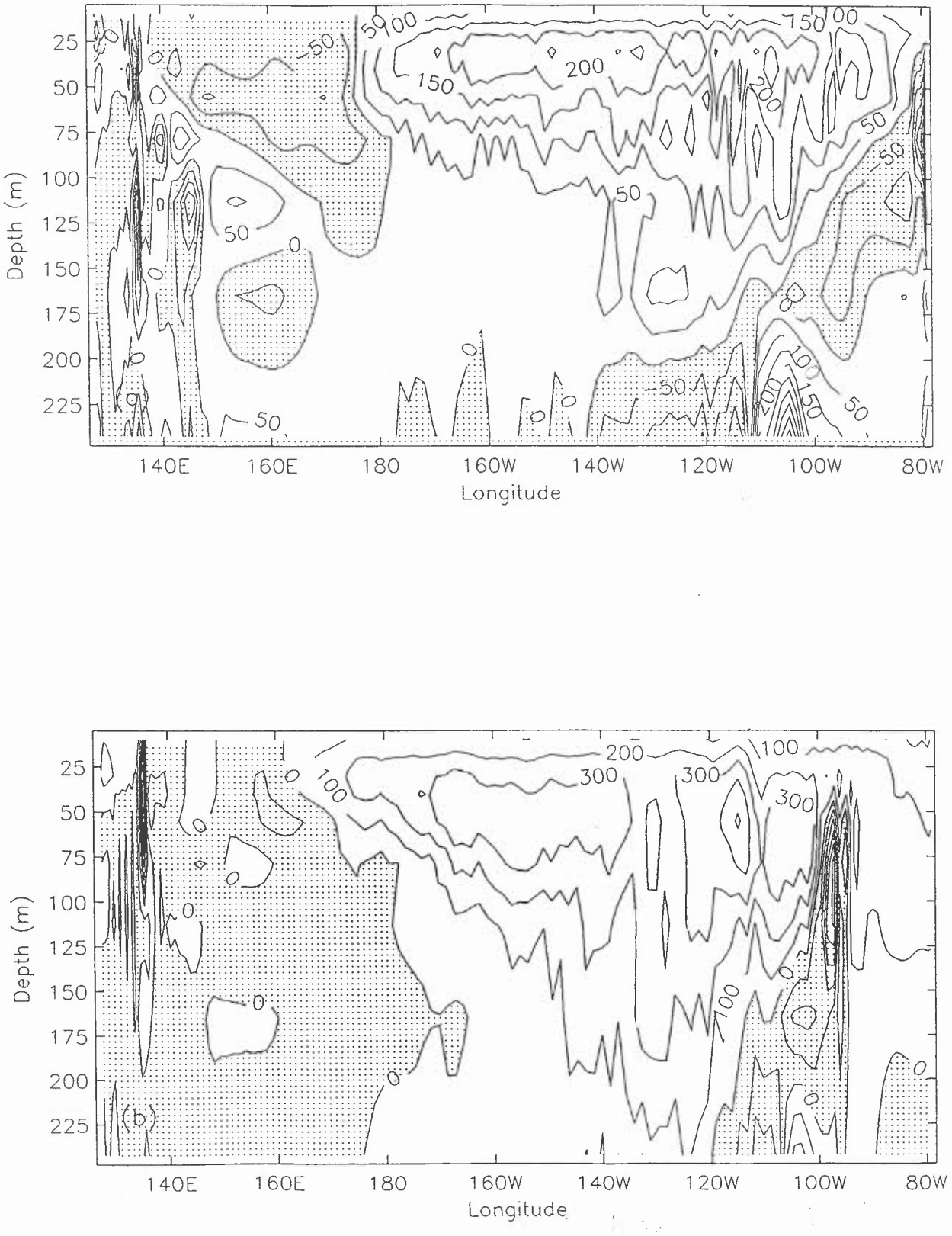

Fig.1 11 GCM : Mean Vertical Velocity (cm per day) at Equator for (a) March (b) September

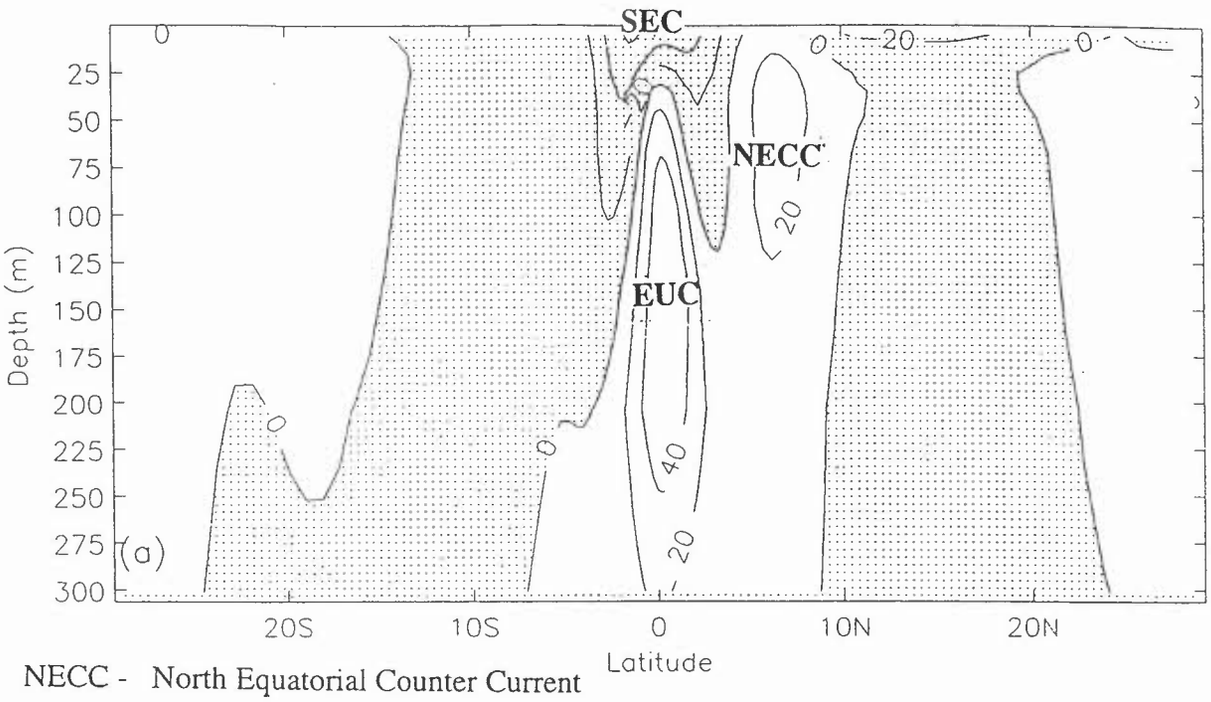

NECC - North Equatorial Counter Current
SEC - South Equatorial Current
EUC - Equatorial Undercurrent

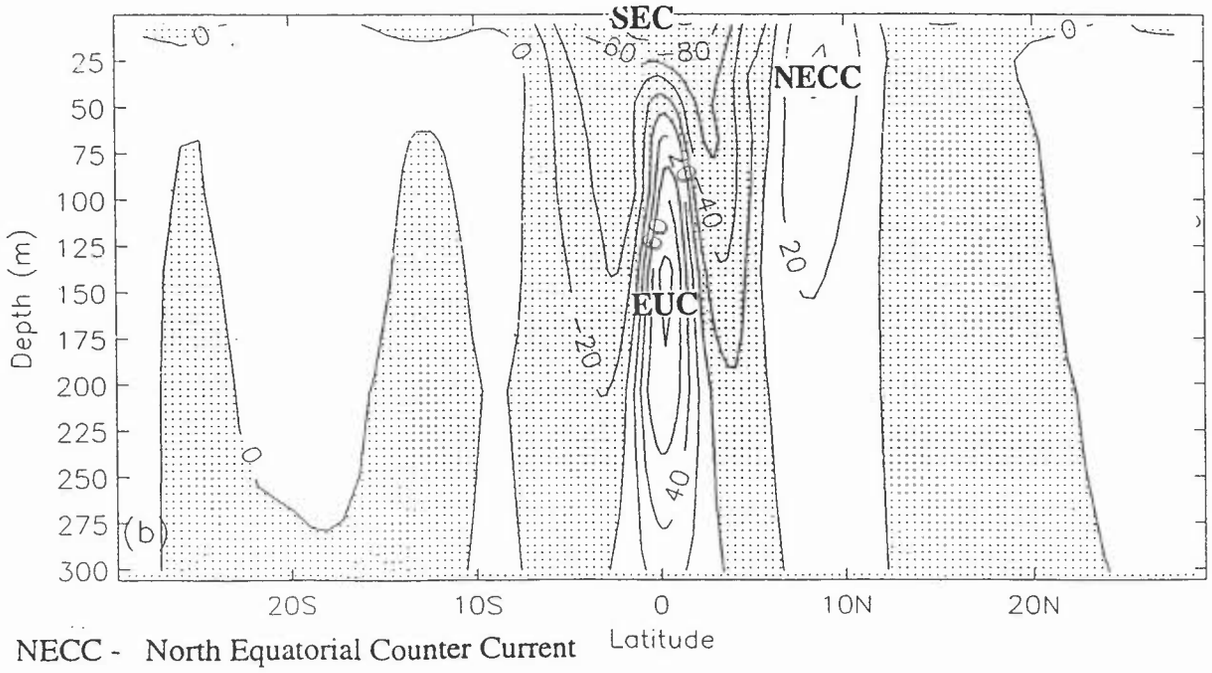

NECC - North Equatorial Counter Current
SEC - South Equatorial Current
EUC - Equatorial Undercurrent

Fig.1.12 GCM : Mean Baroclinic Zonal Velocity (cm/s) at 150°W for (a) March (b) September

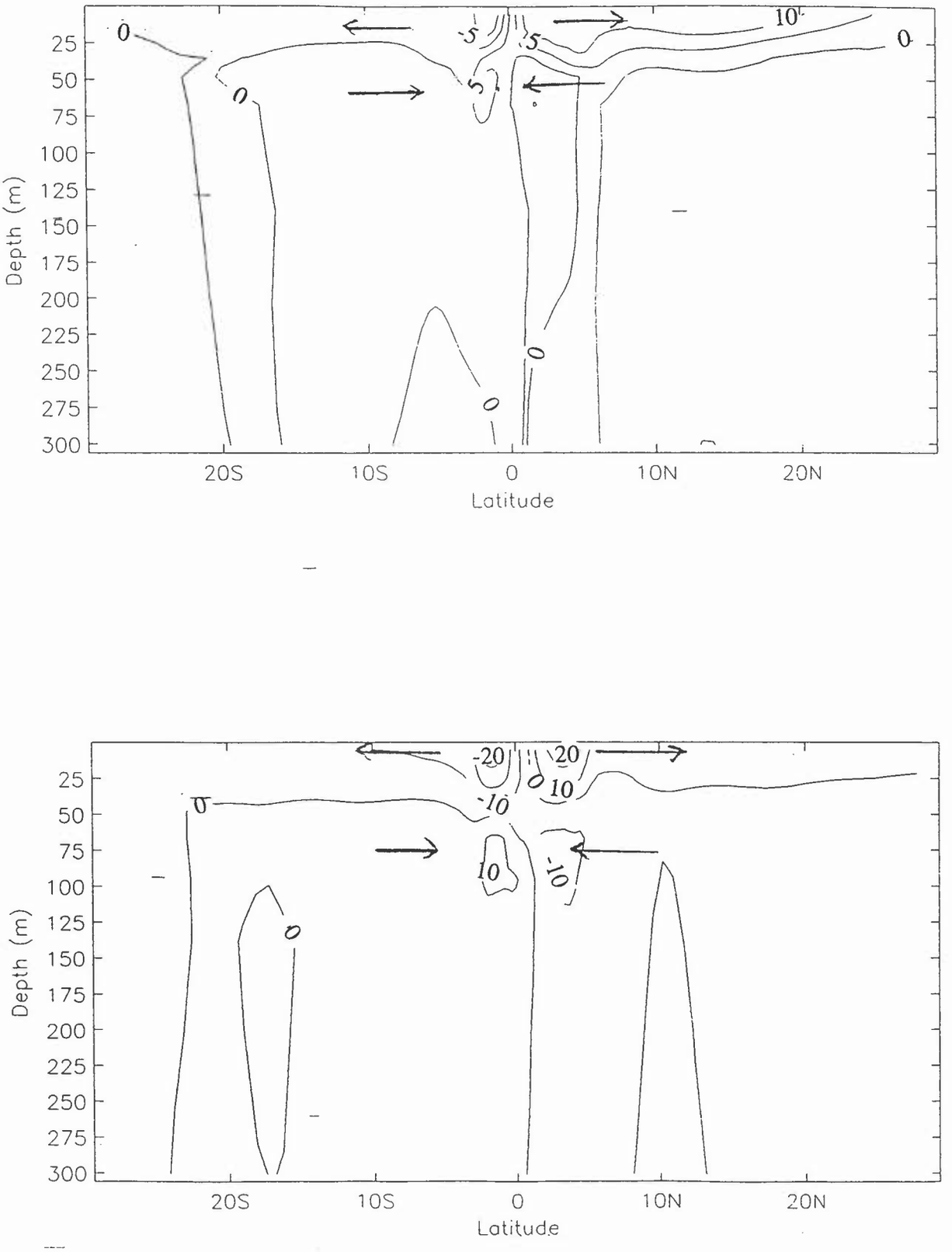

Fig.1.13 GCM : Mean Baroclinic Meridional Velocity (cms^{-1}) at 150°W for (a) March (b) September

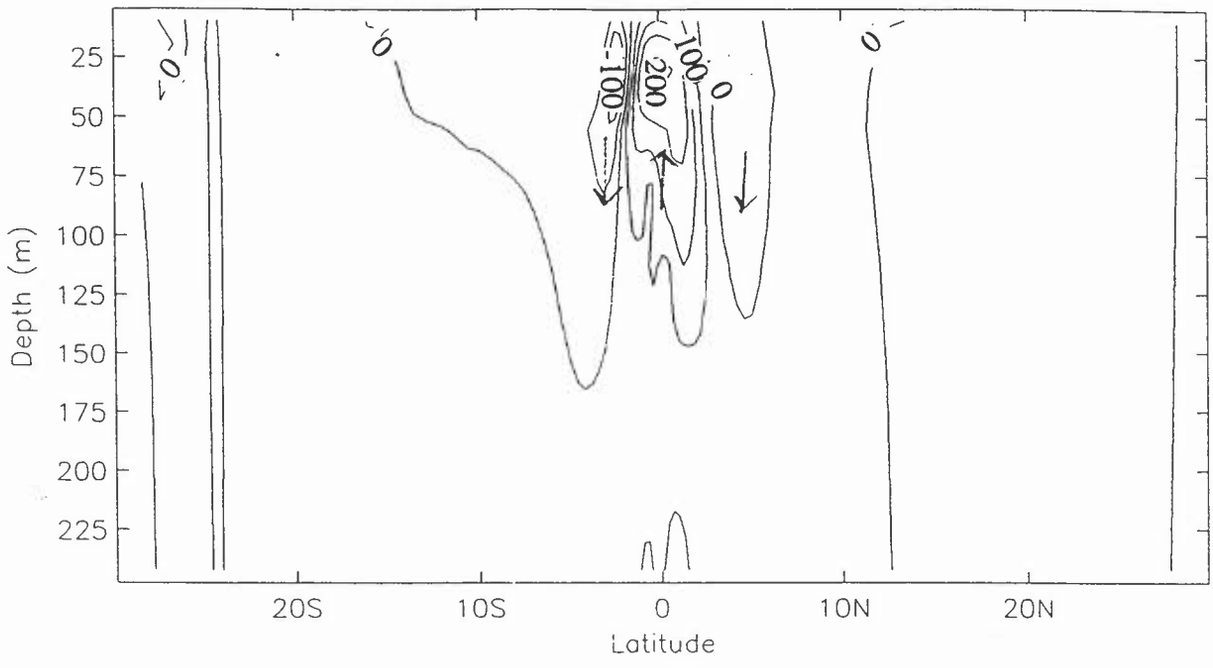

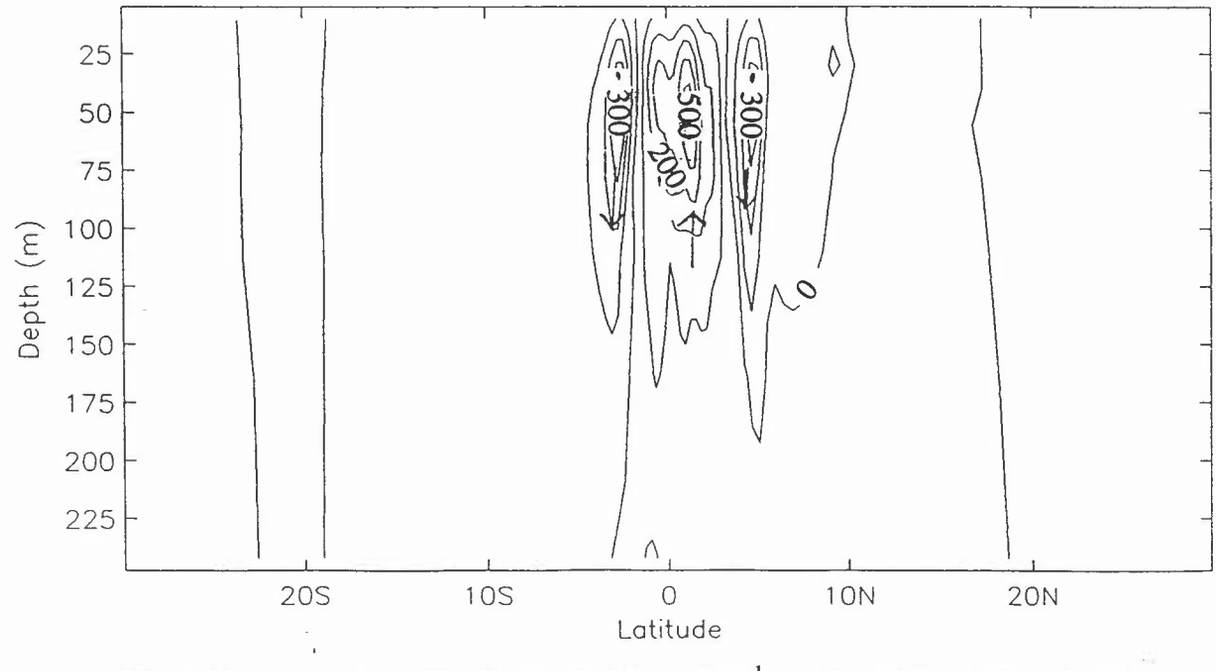

Fig. 1.14 GCM : Mean Vertical Velocity (cmday^{-1}) at 150°W for (a) March (b) September

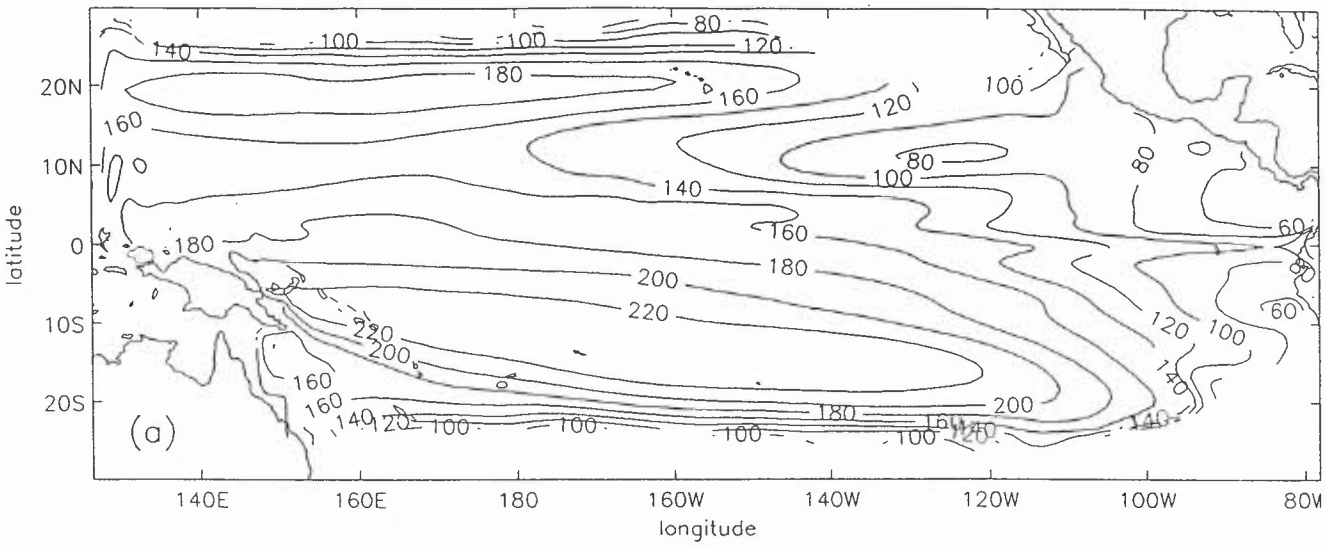

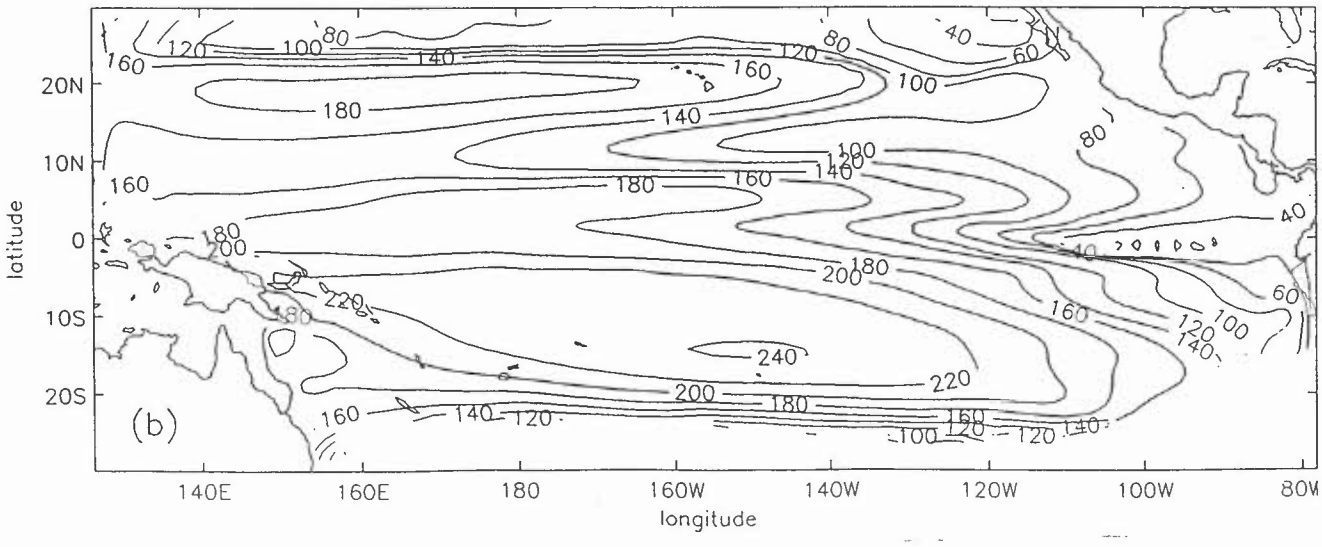

Fig.1.15 GCM : Mean 20 deg.C Isotherm Depth (m) for (a) March and (b) September

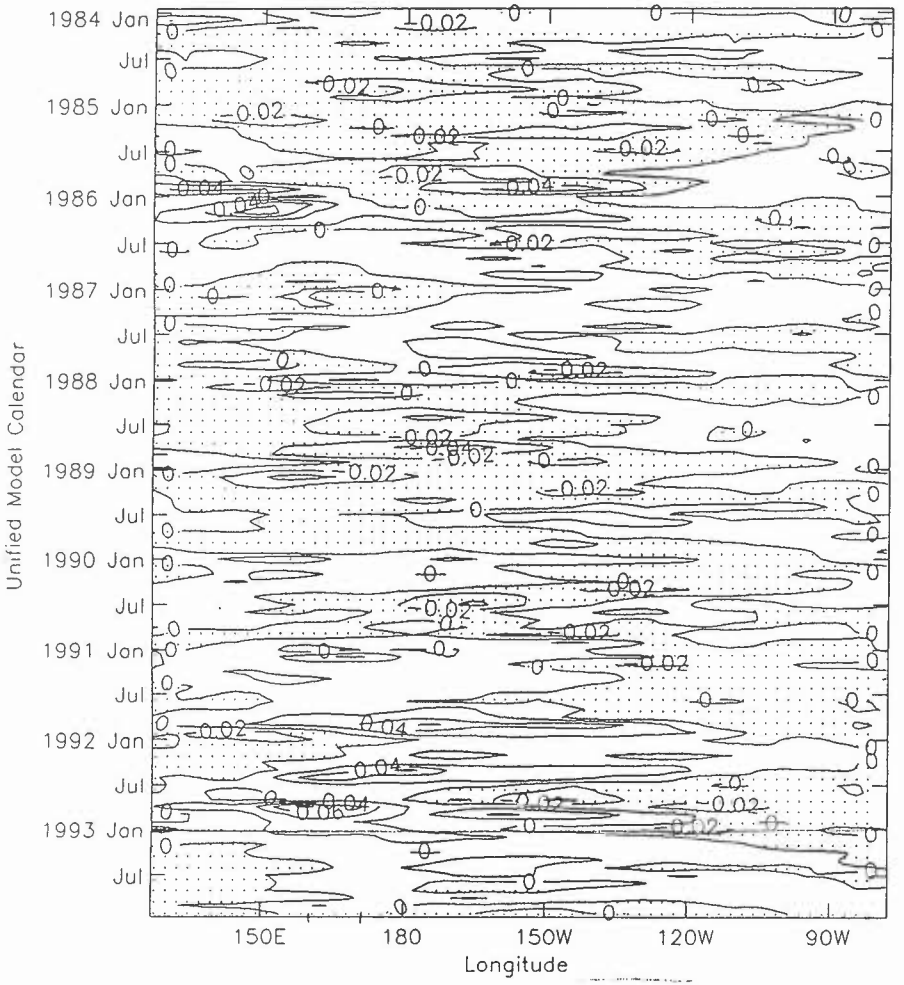

Fig 2.1 Time-longitude Sections of AGCM Taux Anomaly (Nm^{-2}) Along Equator (1984-1993)

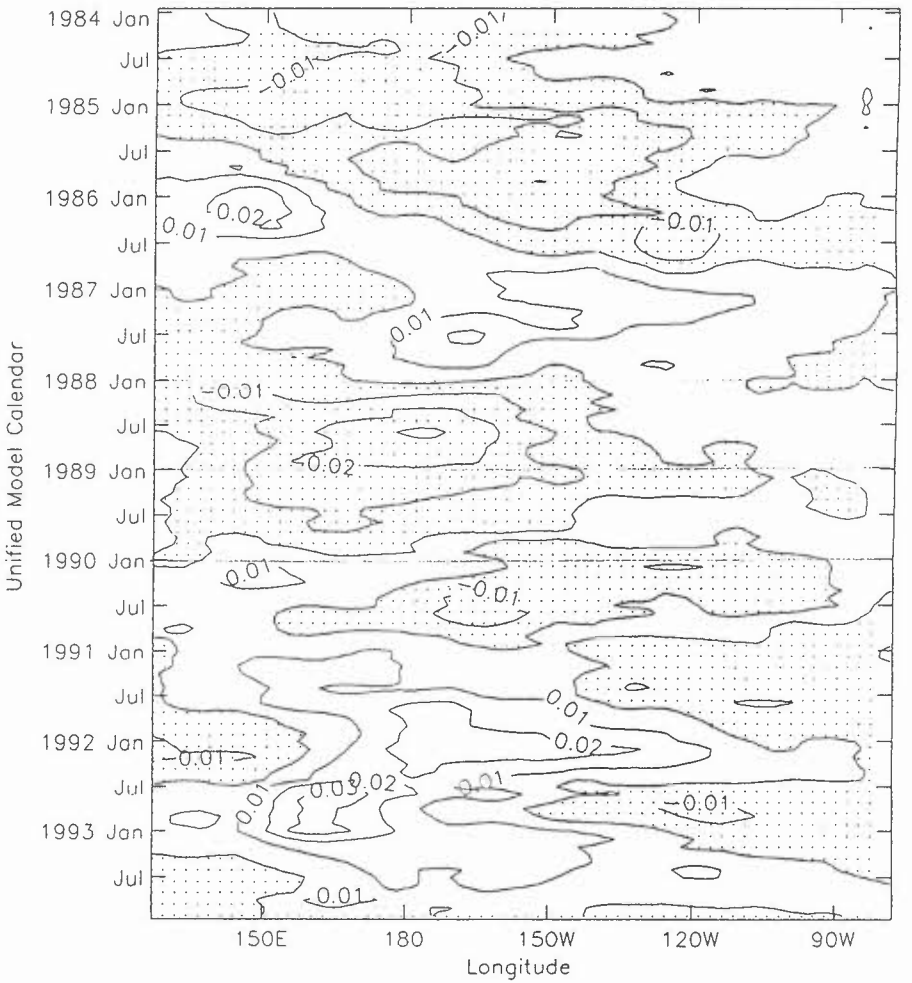

Fig 2.2 Time-longitude Sections of 7 Month Running Mean AGCM Taux Anomaly (Nm^{-2}) Along Equator (1984-1993)

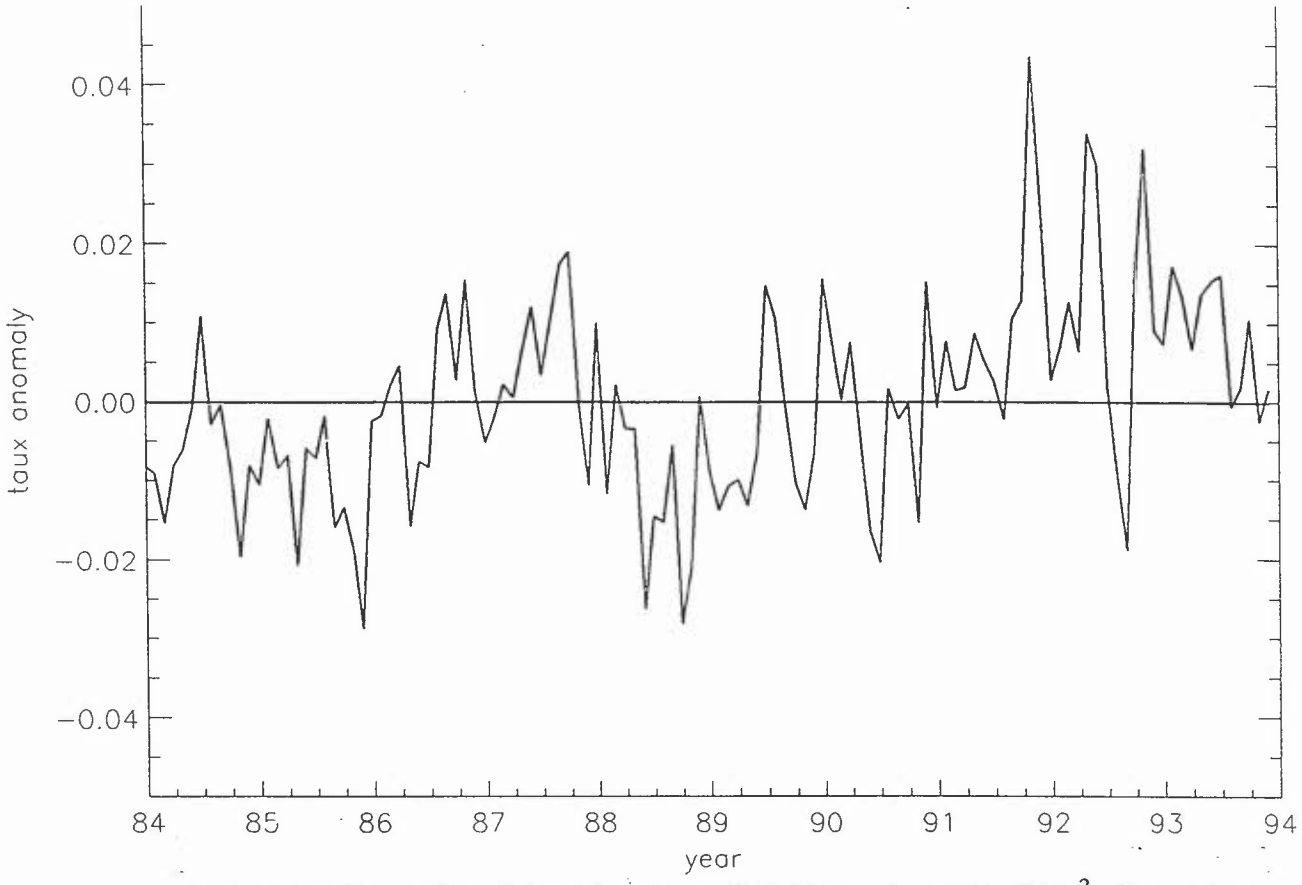

Fig.2.3 Timeseries Plot of Area Average AGCM Taux Anomaly (Nm^{-2}) for Region 5°N-5°S, 165°E-225°E

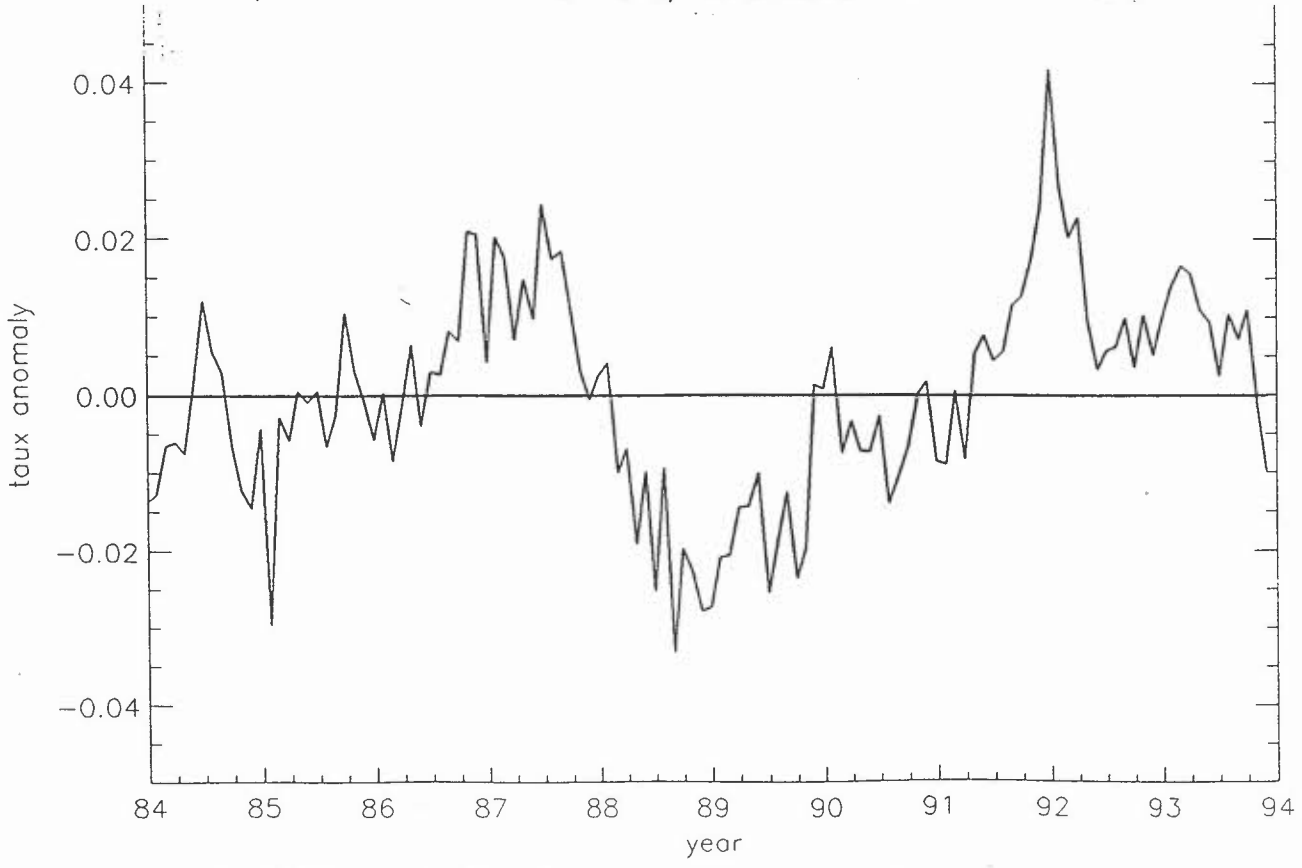

Fig.2.4 Timeseries Plot of Area Average FSU Taux Anomaly (Nm^{-2}) for Region 5°N-5°S, 165°E-225°E

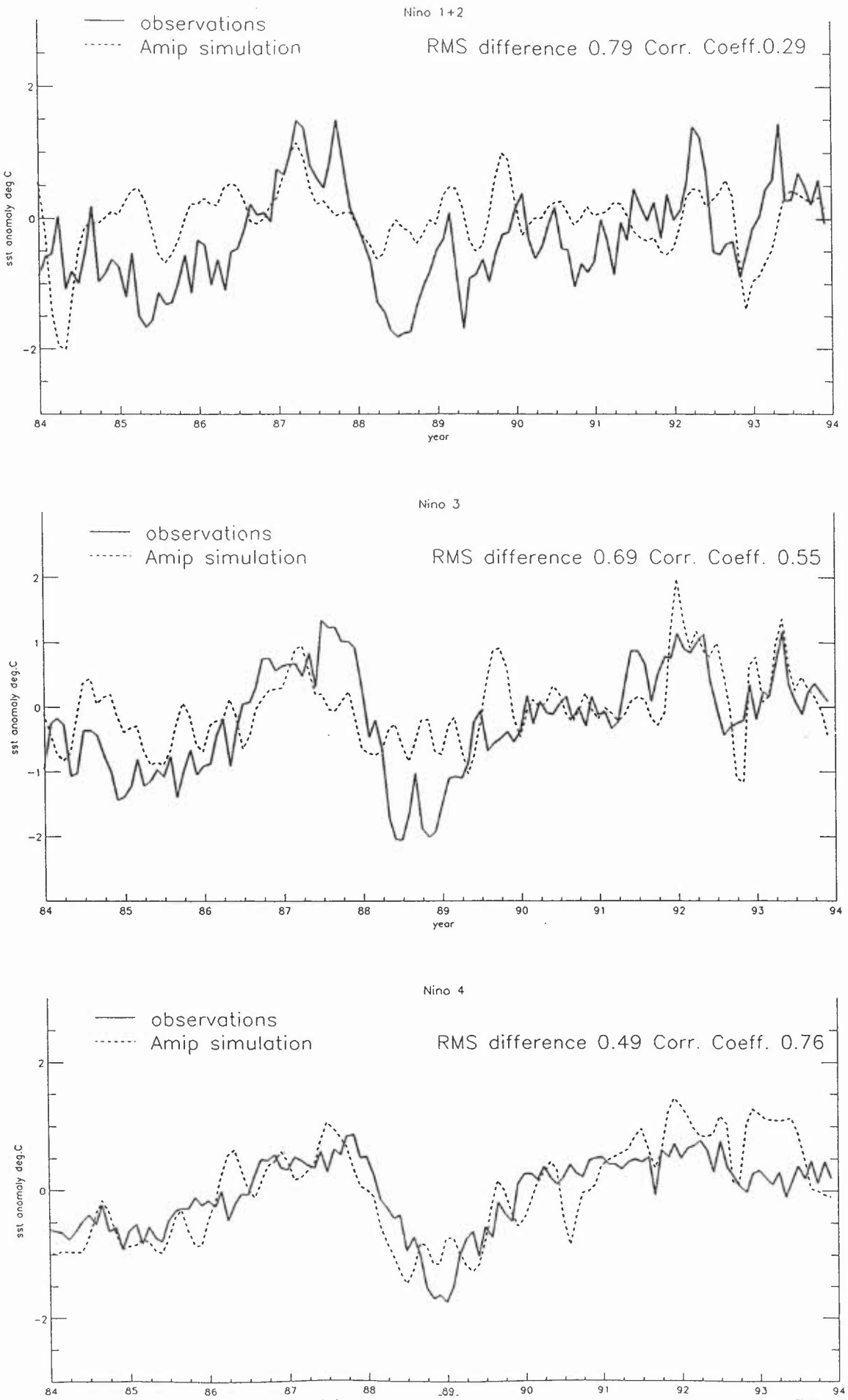

Fig.2.5 Timeseries Plot of Area Average Mean SST Anomaly (°C) for 3 Nino Areas AGCM Simulation Vs Observations

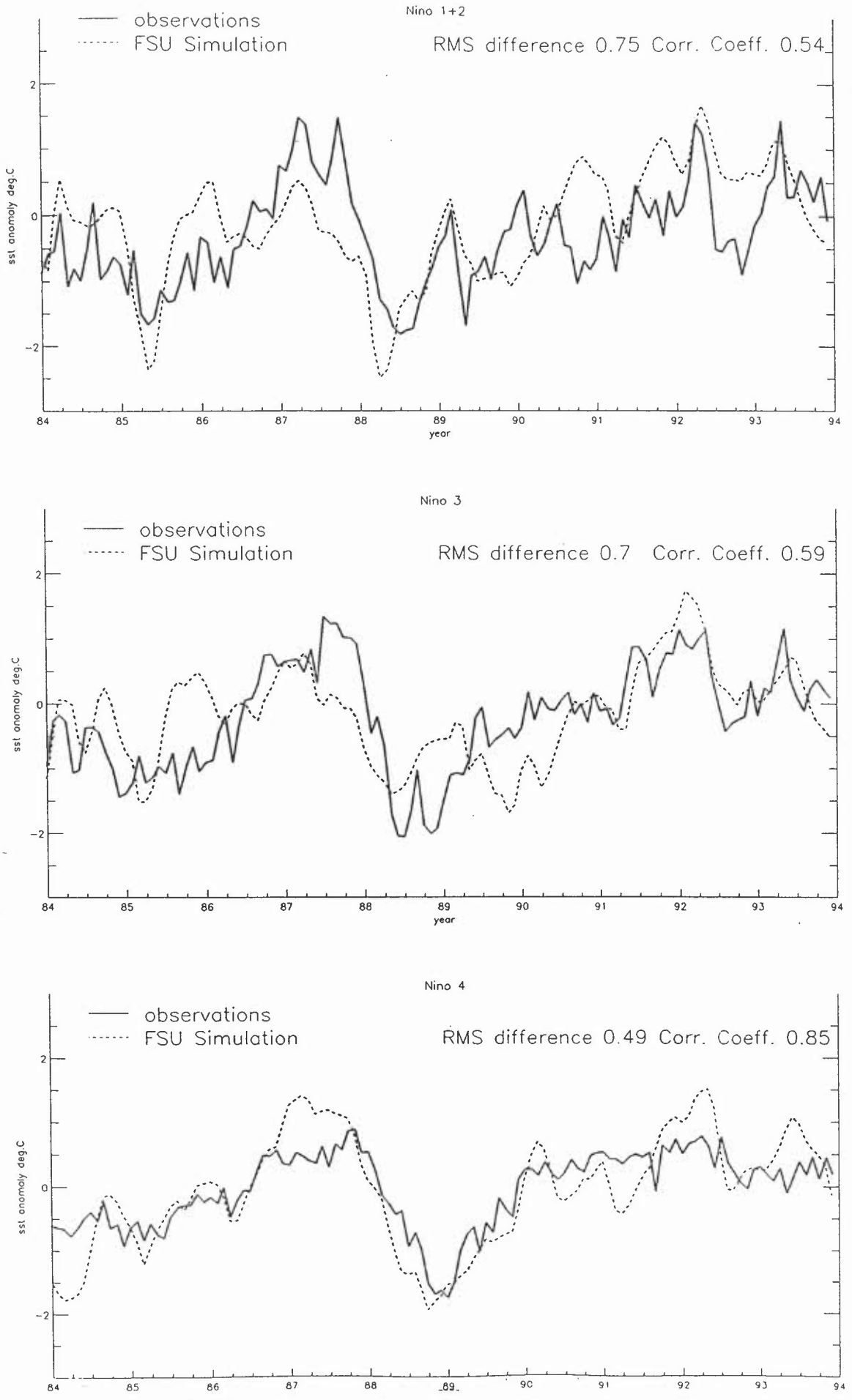

Fig.2.6 Timeseries Plot of Area Averaged Mean SST Anomaly (°C) for 3 Nino Areas FSU Simulation Vs Observations

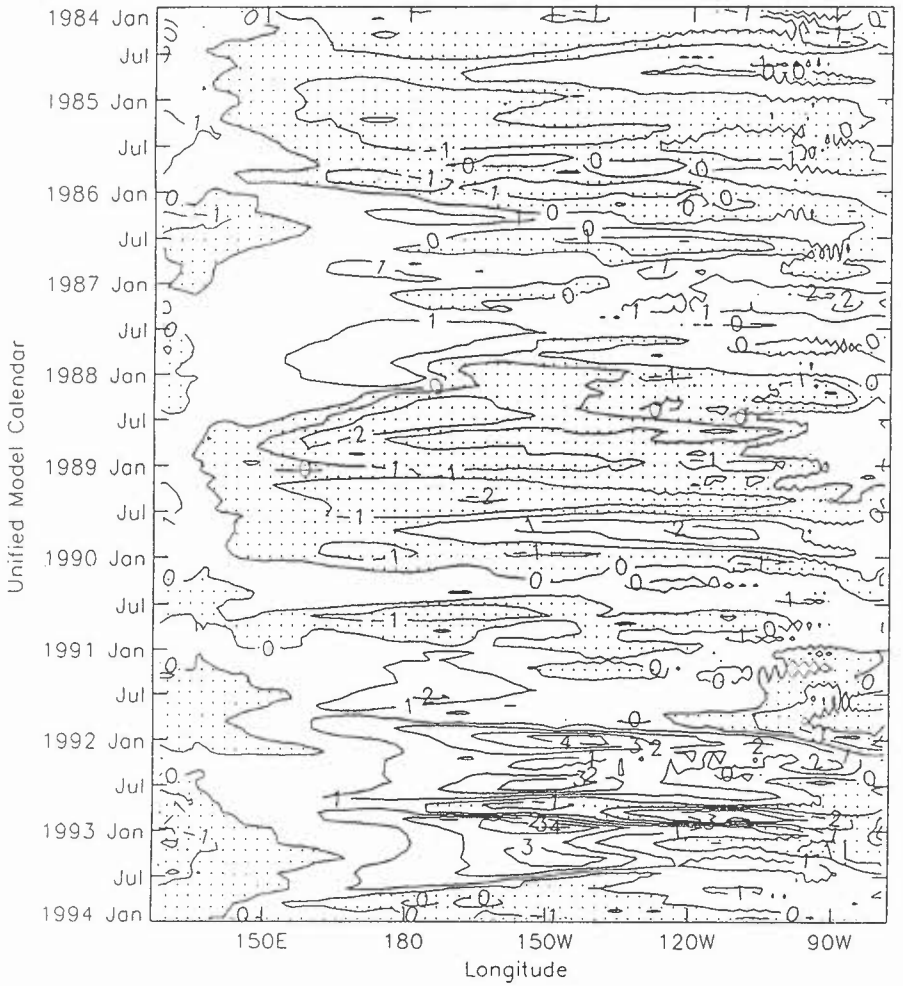

Fig.2.7 Time-longitude Sections of Simulated SST Anomaly (°C) Along Equator (1984-1993)

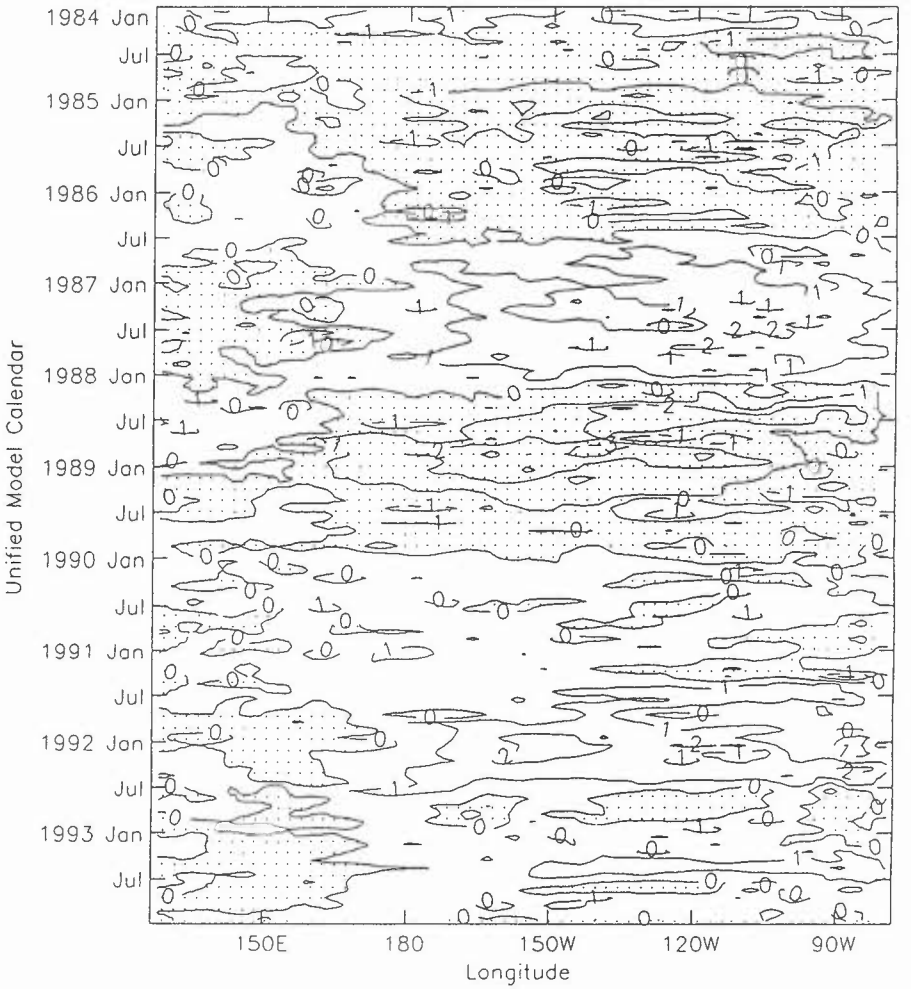

Fig.2.8 Time-longitude Sections of Observed SST Anomaly (°C) Along Equator (1984-1993)

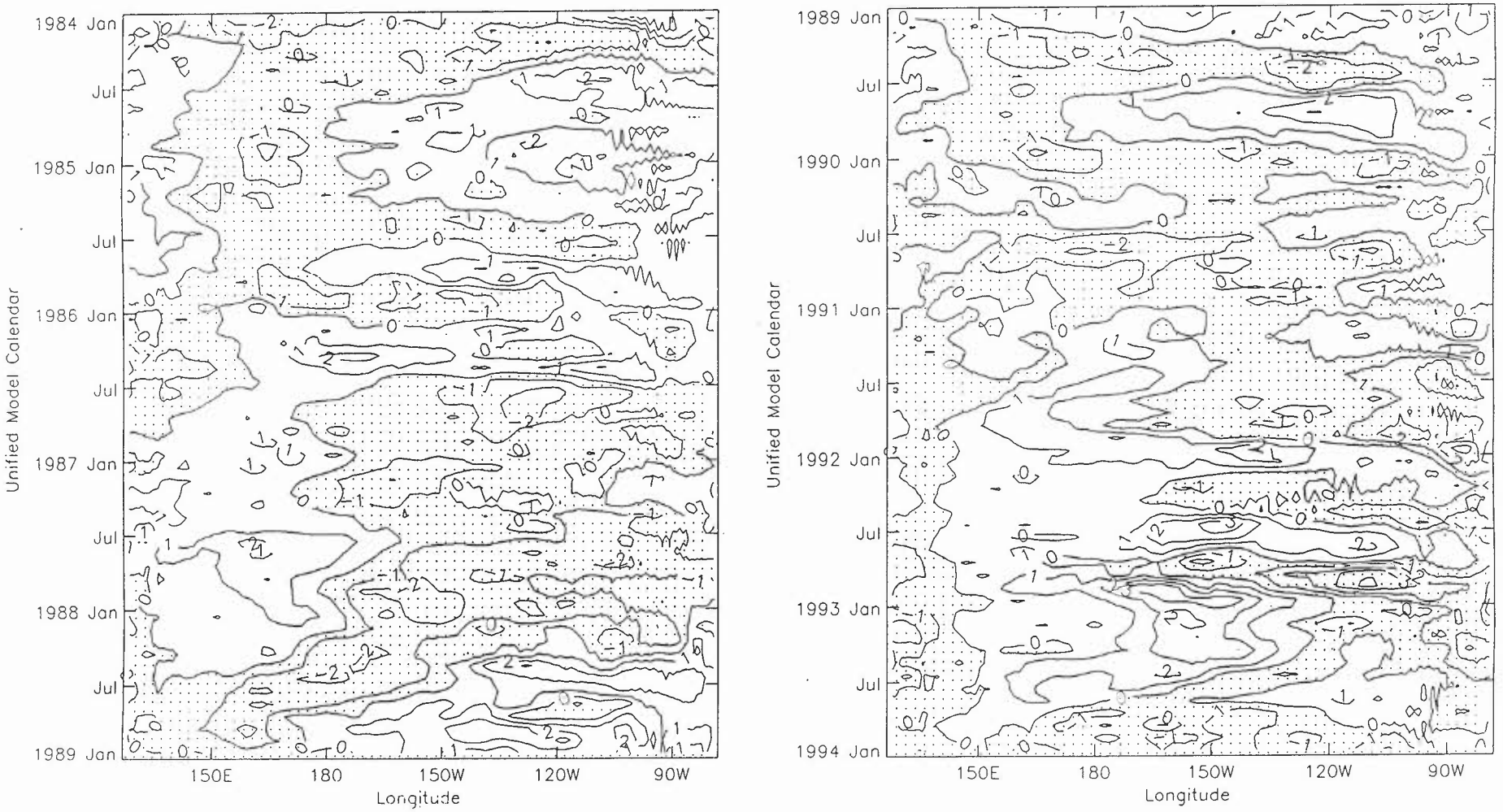

Fig 2.9 Time-longitude Sections of Simulated - Observed SST Anomaly Along Equator (1984-1993)

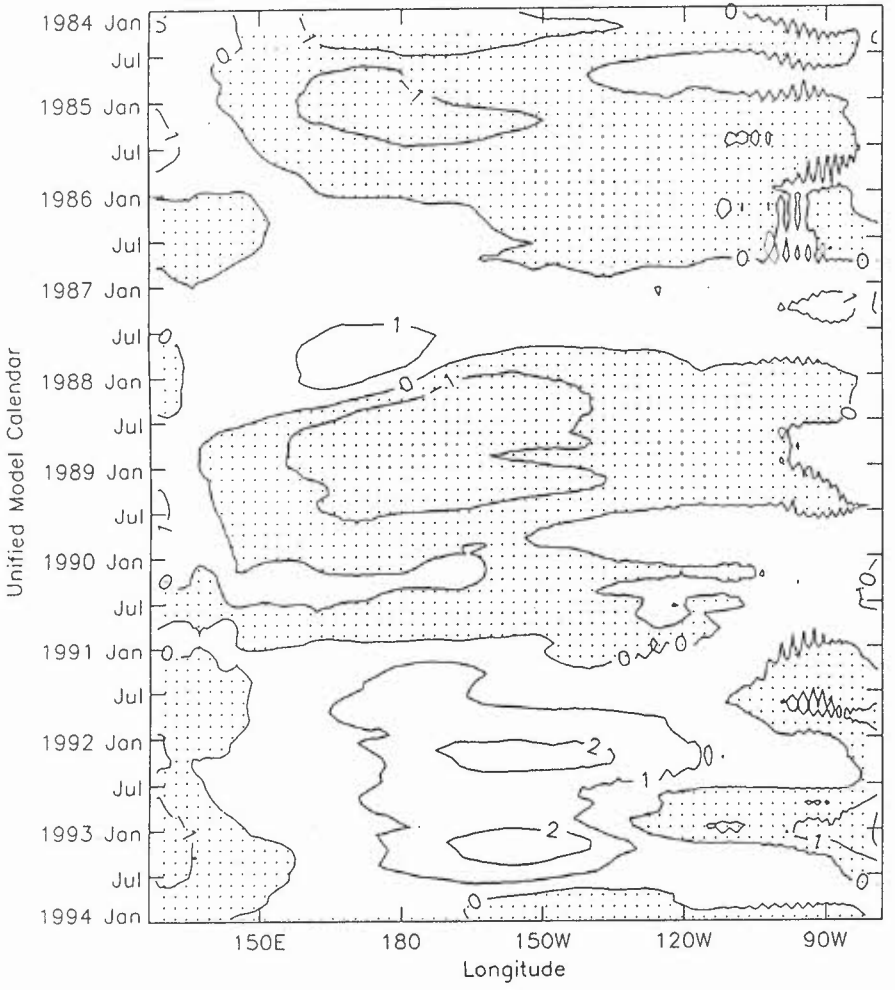

Fig 2.10 Time-longitude Sections of 7 Month Running Mean of Simulated SST Anomaly (°C) Along Equator (1984-1993)

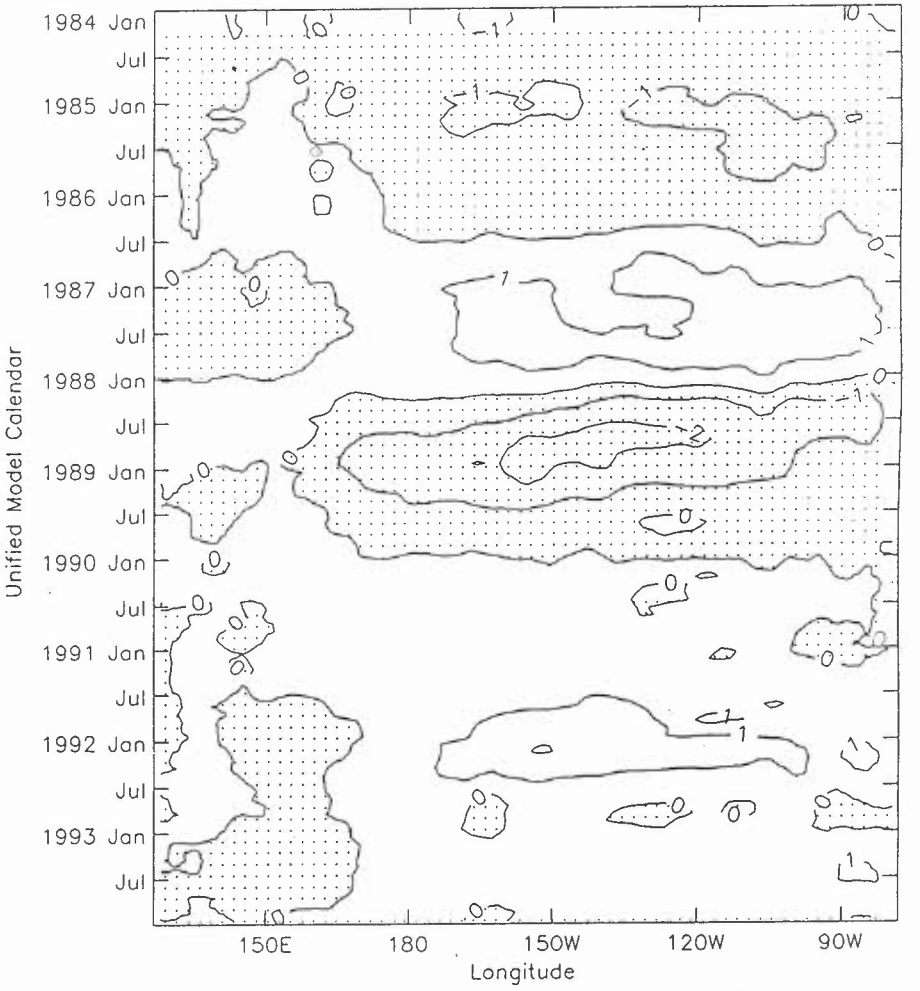

Fig 2.11 Time-longitude Sections of 7 Month Running Mean of Observed SST Anomaly (°C) Along Equator (1984-1993)

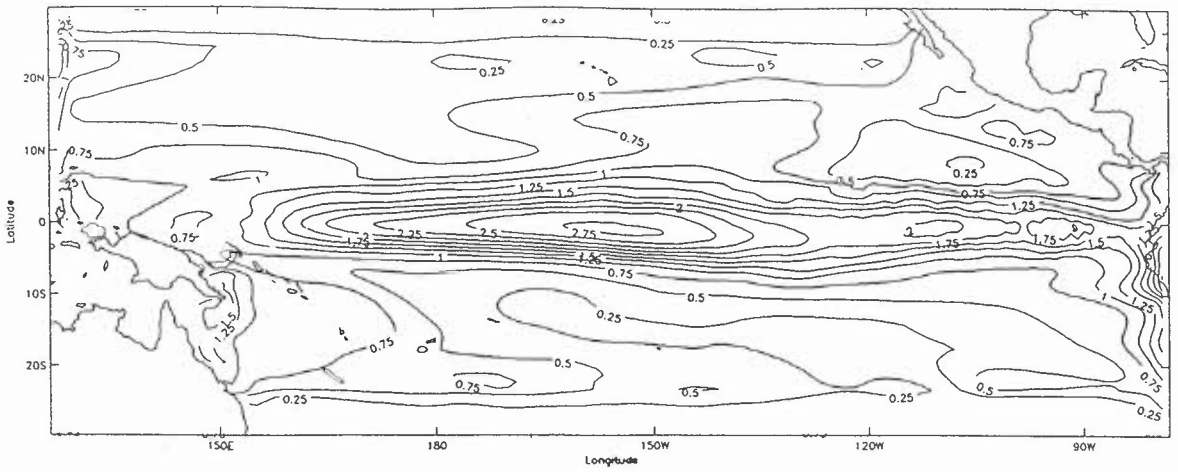

Fig.2.12 Standard Deviation of SST Anomaly (°C) for the AGCM Forced Simulation (1984-93)

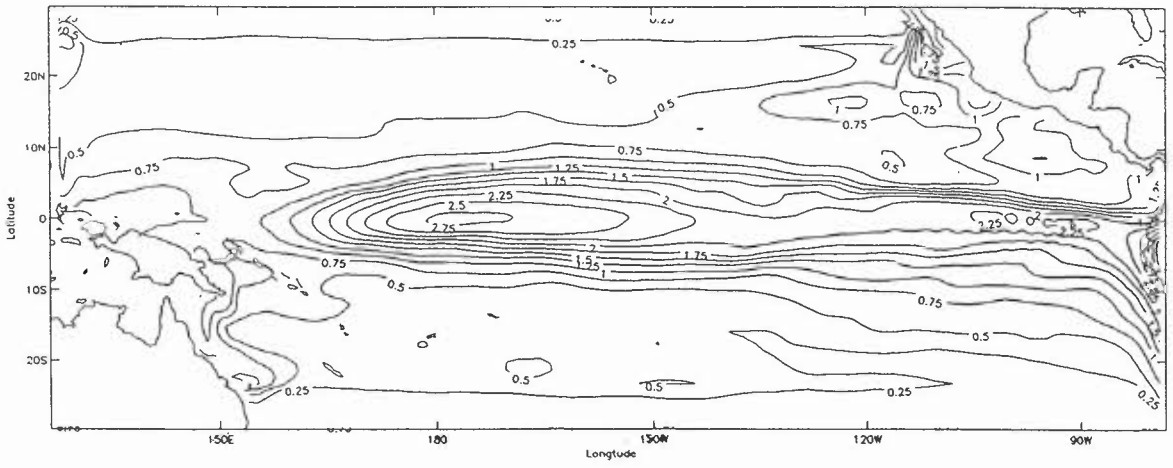

Fig.2.13 Standard Deviation of SST Anomaly (°C) for the FSU Forced Simulation (1984-93)

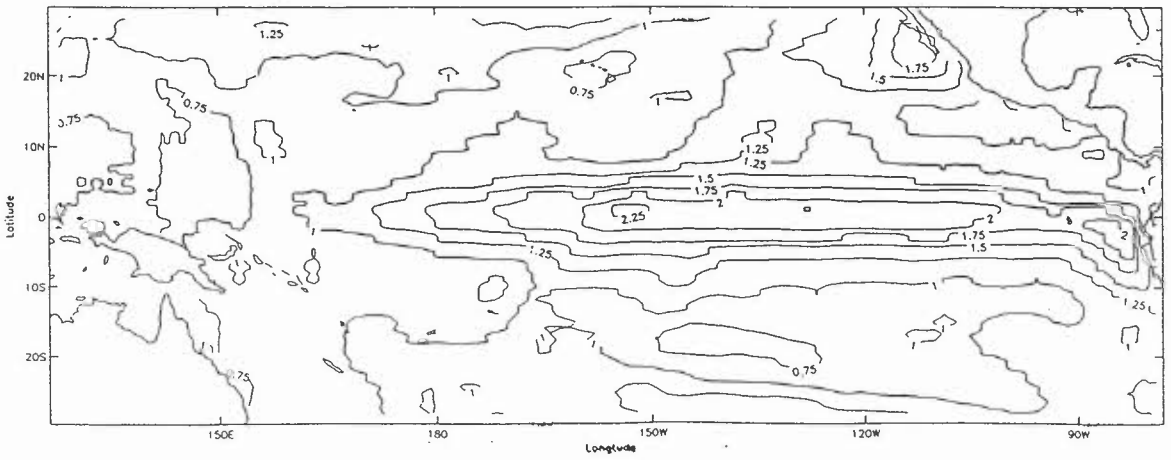

Fig.2.14 Standard Deviation of Observed SST Anomaly (°C) (1984-93)

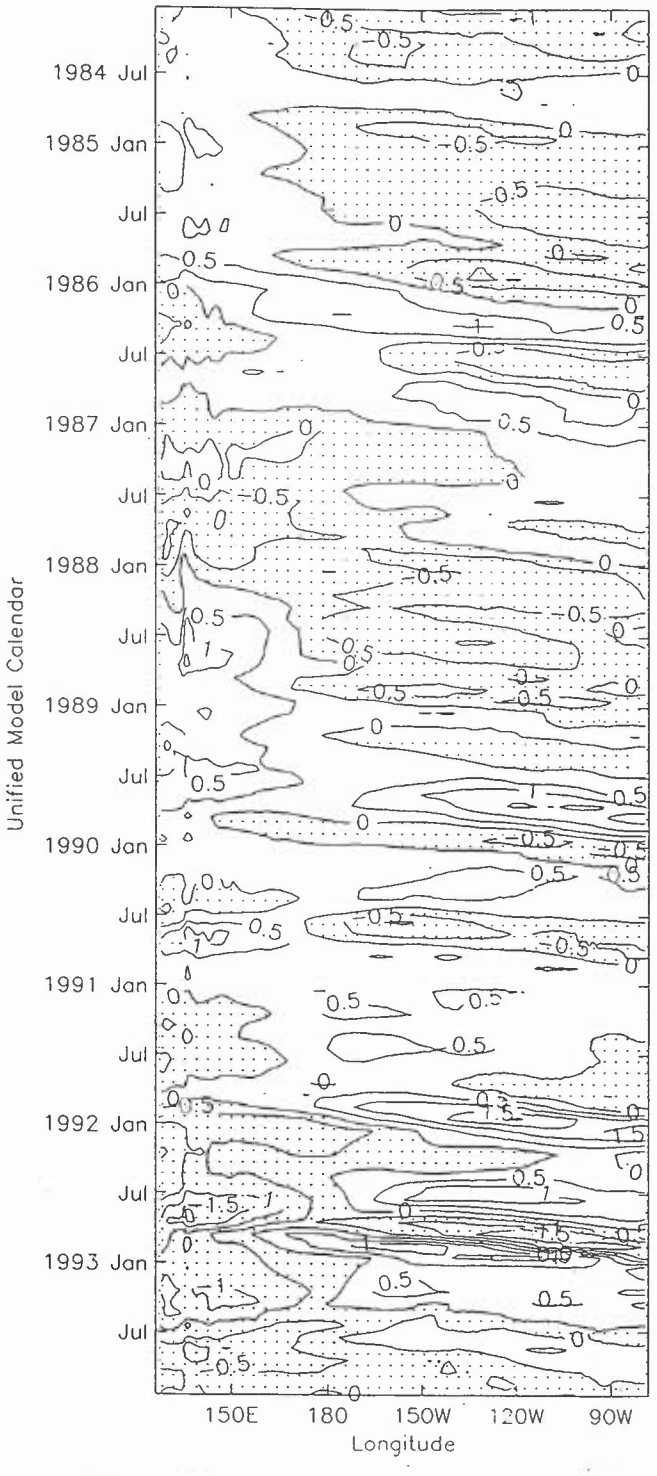

Fig 2.15 Time-longitude Sections of Simulated Heat Content Anomaly (°C) Along Equator (1984-1993)

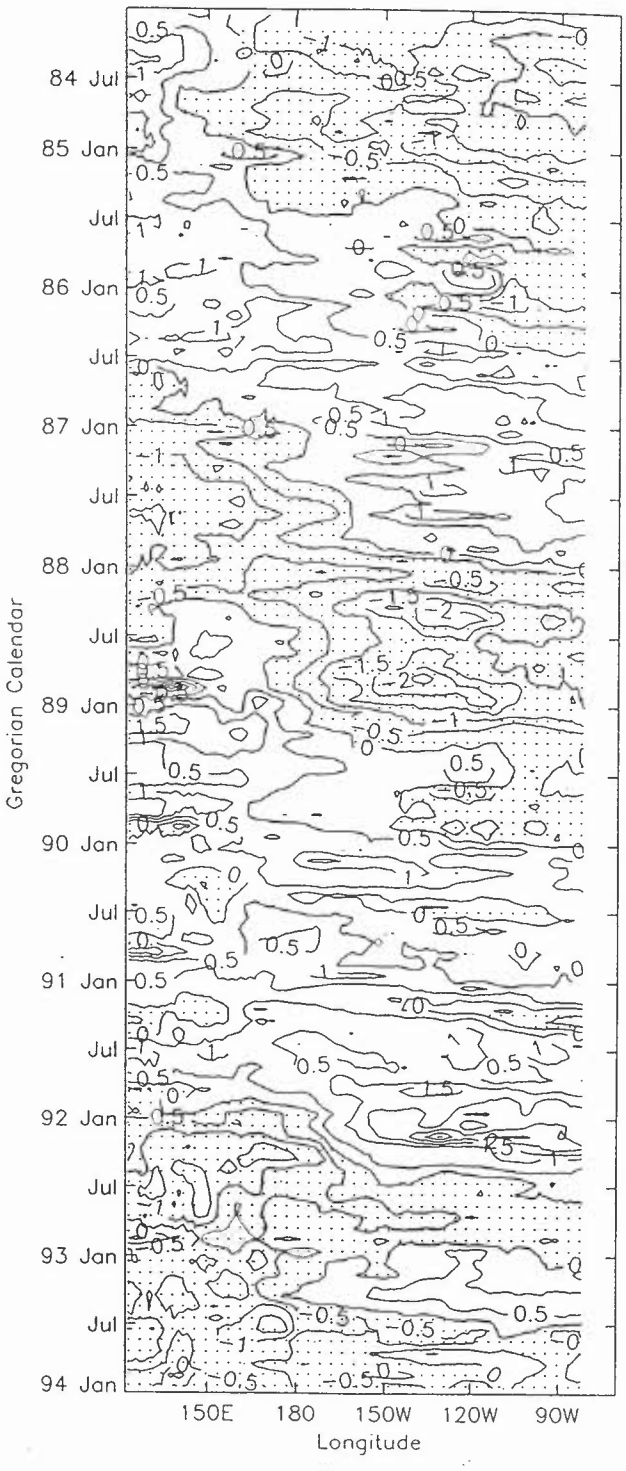

Fig 2.16 Time-longitude Sections of NMC Analysis Heat Content Anomaly (°C) Along Equator (1984-1993)

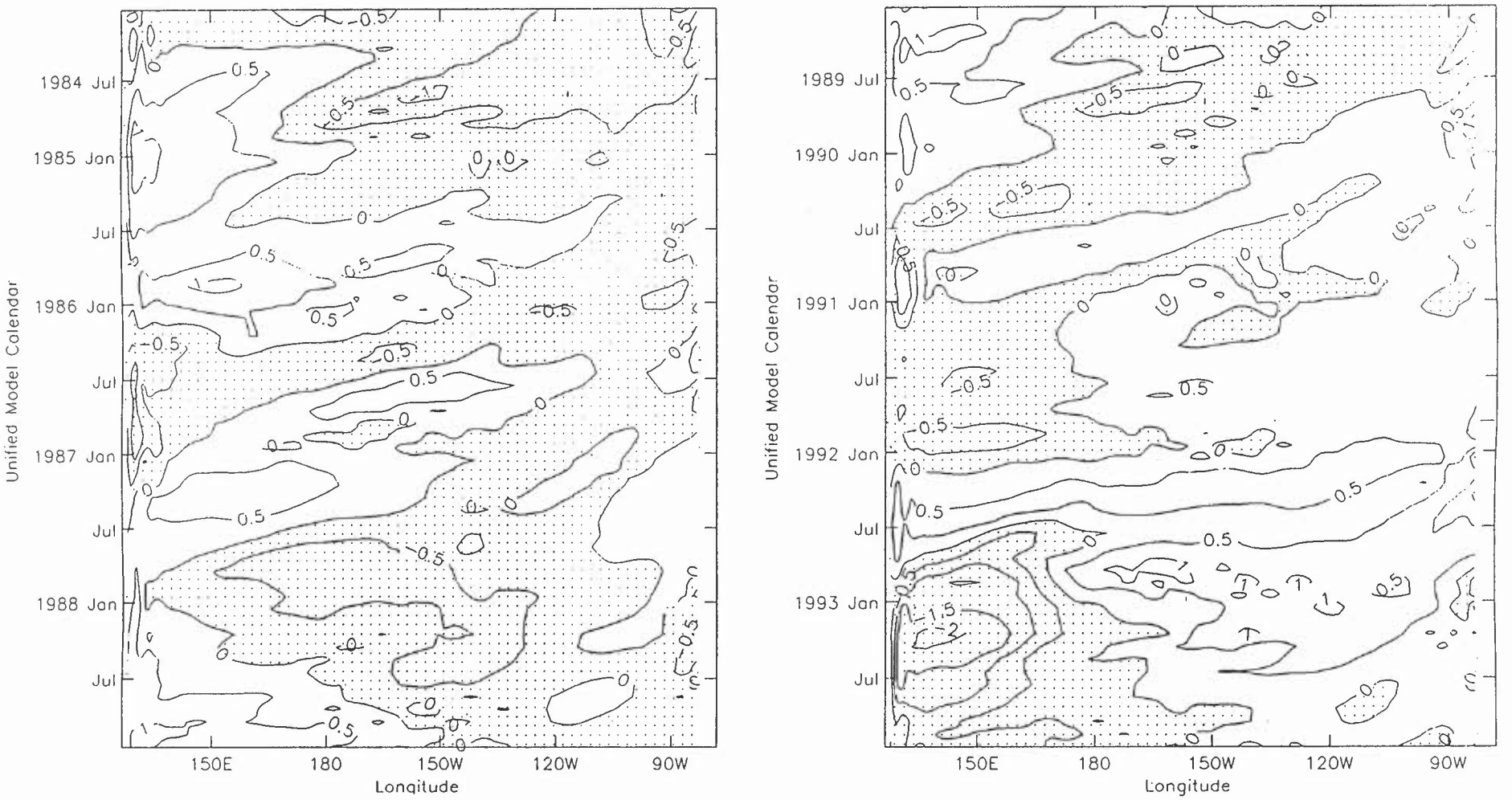

Fig 2.17 Time-longitude Sections of Simulated Heat Content Anomaly (°C) Along 8°N (1984-1993)